



## Fe-bearing phases in modern lacustrine microbialites from Mexico

Nina Zeyen, Karim Benzerara, Nicolas Menguy, Jessica Brest, Alexis Templeton, Samuel Webb, Emmanuelle Gérard, David Moreira, Purificación López-García, Rosaluz Tavera, et al.

### ► To cite this version:

Nina Zeyen, Karim Benzerara, Nicolas Menguy, Jessica Brest, Alexis Templeton, et al.. Fe-bearing phases in modern lacustrine microbialites from Mexico. *Geochimica et Cosmochimica Acta*, 2019, 253, pp.201-230. 10.1016/j.gca.2019.03.021 . hal-02124836

**HAL Id: hal-02124836**

**<https://hal.sorbonne-universite.fr/hal-02124836>**

Submitted on 9 May 2019

**HAL** is a multi-disciplinary open access archive for the deposit and dissemination of scientific research documents, whether they are published or not. The documents may come from teaching and research institutions in France or abroad, or from public or private research centers.

L'archive ouverte pluridisciplinaire **HAL**, est destinée au dépôt et à la diffusion de documents scientifiques de niveau recherche, publiés ou non, émanant des établissements d'enseignement et de recherche français ou étrangers, des laboratoires publics ou privés.

# Fe-bearing phases in modern lacustrine microbialites from Mexico

Nina Zeyen<sup>1,2</sup>, Karim Benzerara<sup>1,\*</sup>, Nicolas Menguy<sup>1</sup>, Jessica Brest<sup>1</sup>, Alexis S. Templeton<sup>3</sup>, Samuel M. Webb<sup>4</sup>, Emmanuelle Gérard<sup>5</sup>, David Moreira<sup>6</sup>, Purificación López-García<sup>6</sup>, Rosaluz Tavera<sup>7</sup>, Guillaume Morin<sup>1</sup>

<sup>1</sup> *Institut de Minéralogie, de Physique des Matériaux et de Cosmochimie, IMPMC, UMR CNRS 7590, Sorbonne Université, Muséum National d'Histoire Naturelle, IRD, 75252 Paris cedex 05, France*

<sup>2</sup> *Now at Department of Earth and Atmospheric Sciences, University of Alberta, Edmonton, AB T6G 2E3, Canada*

<sup>3</sup> *Department of Geological Sciences, UCB 399, University of Colorado, Boulder, CO 80309, USA*

<sup>4</sup> *Stanford Synchrotron Radiation Lightsource, Stanford University, Menlo Park, CA 94025, USA*

<sup>5</sup> *IPGP, Sorbonne Paris Cité, UMR 7154, Université Paris Diderot, CNRS, Paris, France*

<sup>6</sup> *Unité d'Ecologie, Systématique et Evolution, CNRS UMR 8079, Université Paris-Sud, Orsay, France*

<sup>7</sup> *Departamento de Ecología y Recursos Naturales, Universidad Nacional Autónoma de México, DF México, México*

\* Corresponding author

Tel.: +33(0)144277542

E-mail address: [karim.benzerara@upmc.fr](mailto:karim.benzerara@upmc.fr)

**Keywords:** microbialites; layered double hydroxides; iowaite; pyroaurite; authigenesis; Fe-bearing talc; stevensite; hydromagnesite

**In revision**

*Geochimica et Cosmochimica Acta*

## ABSTRACT

Transition metal ions impurities in microbialites have been previously suggested as paleoenvironmental and/or paleobiological proxies. However, how metals are incorporated into microbialites remains poorly known. Here, in order to assess the distribution and speciation of Fe in modern microbialites, we conducted bulk x-ray diffraction, infrared spectroscopy, x-ray absorption near-edge structure (XANES) spectroscopy, electron microscopy and x-ray microscopy analyses on samples collected from shallow depths in five alkaline lakes in Mexico: Lake Alchichica, Lake La Preciosa, Lake Atexcac, Lake La Alberca de Los Espinos and Lake Pátzcuaro. A range of Fe contents were measured in these microbialites, from low (~0.12 wt.%) to relatively high (~2.2 wt.%). Fe was distributed heterogeneously in microbialites, mostly localized as hotspots or sometimes arranged as discrete laminae. Fe was mostly trivalent in all microbialites and was incorporated into diverse authigenic phases, the proportion of which varied among microbialites. Authigenic phases included Fe-bearing Mg-phyllsilicates such as kerolite and/or stevensite, i.e.  $(\text{Mg,Fe(II),Fe(III)})_3\text{Si}_4\text{O}_{10}(\text{OH})_2 \cdot n\text{H}_2\text{O}$  and Fe-Mg layered double hydroxides (LDH), i.e. pyroaurite  $[\text{Mg(II)}_6\text{Fe(III)}_2(\text{CO}_3)(\text{OH})_{16} \cdot 4\text{H}_2\text{O}]$  and/or iowaite  $[\text{Mg(II)}_6\text{Fe(III)}_2\text{Cl}_2(\text{OH})_{16} \cdot 4\text{H}_2\text{O}]$ , together with Fe-(oxyhydr)oxides. Carbonate phases were negligible carriers of Fe in all lakes. Iowaite/pyroaurite phases, which have often been found as low temperature alteration products in serpentinites, were surprisingly observed in Lake Alchichica, whereas Fe-bearing kerolite/stevensite was present in Lake La Preciosa, Lake Atexcac, Lake La Alberca de Los Espinos and Lake Pátzcuaro. Fe present in these shallow water microbialites may be originated from groundwater seepage derived from adjacent Fe-rich volcanic rocks. We suggest that the occurrence of iowaite/pyroaurite vs authigenic Fe-bearing kerolite/stevensite depends on the orthosilicic acid concentration in the lakes.

Pyroaurite/iowaite may form and stay preserved in Lake Alchichica because of the low  $[\text{H}_4\text{SiO}_4]$  as well as high alkalinity,  $[\text{Mg}^{2+}]$ ,  $[\text{CO}_3^{2-}]$ ,  $[\text{Cl}^-]$  and pH ( $\sim 9$ ) prevailing in this lake, while in other lakes, where  $[\text{H}_4\text{SiO}_4]$  is higher (above  $\sim 0.4$  mM), Fe-bearing kerolite or smectite phases are formed. Overall, the message carried by the Fe-bearing mineral phases in these modern microbialites is multifold: Fe-bearing phases within microbialites may contain some information on environmental conditions (e.g.,  $[\text{H}_4\text{SiO}_4]$ ) as well as on geochemical processes implicated during their formation (e.g., seepage of anoxic Fe-bearing groundwater). Considering the reactivity of pyroaurite/iowaite and kerolite/stevensite and their possible transformation into diverse mineral phases upon microbial activity, burial and diagenesis, a careful appraisal of Fe speciation using a similar combination of bulk and microscopy analyses is required in order to better assess the origin of Fe in ancient microbialites.

## 1. INTRODUCTION

Microbialites are organo-sedimentary rocks formed in close association with microorganisms (Burne and Moore, 1987). These rocks have been repeatedly suggested to record information on the environmental conditions under which they formed (e.g., Chagas et al., 2016). Part of this information can be retrieved through the analysis of their chemical composition, including their trace and/or transition element content (Petrash et al., 2016). For example, some modern microbialites have been shown to retain shale-normalized rare earth element ( $\text{REE}_{\text{SN}}$ ) patterns similar to those of seawater, suggesting that ancient microbialites may be used to infer past chemical variations of seawater (Webb and Kamber, 2000). Alternatively, the trace element and transition metal content in microbialites may be impacted by some biological fractionation processes and provide information on past microbial activities (Kamber and Webb, 2007). The trace element chemical patterns may also be



modified secondarily by diagenetic processes, as shown for some ca 1.88 Ga old stromatolites from the Gunflint Formation (Petrash et al., 2016).

The Fe chemistry in microbialites has been specifically investigated as a potential source of paleoenvironmental information. For example, Von Blanckenburg et al. (2008) suggested that most of Fe found in some modern and ancient marine microbialites occurred in hydrogenous carbonates, rather than Fe and Mn-hydroxides. If this were true, the Fe isotope composition of ancient microbialites could be used to record ancient seawater Fe chemistry. Alternatively, Fe can be actively processed and transformed by diverse microorganisms, serving as an electron donor or acceptor for various microbial metabolisms and/or as a co-factor for several enzymes (e.g., Weber et al., 2006; Cornelis, 2014). For example, Planavsky et al. (2009) interpreted the Fe isotope composition of 1.89 Ga old microbialites as the result of microbially-mediated Fe precipitation involving Fe-oxidizing bacteria. Overall, there is a need to better understand how Fe becomes sequestered within microbialites.

Modern microbialites may form differently from ancient microbialites, especially from the Archean. Therefore, great care should be taken when applying interpretations from the modern to the past (e.g., Bosak et al., 2013). Yet the study of metal chemistry in modern microbialites may serve as a model case to better assess the complex processes involved in Fe sequestration within microbialites and the diversity of primary Fe-bearing mineral phases that may form. Fe was sometimes abundant in ancient microbialites, especially when ferruginous conditions were prevailing in aqueous environments (e.g., Von Blanckenburg et al., 2008). In contrast, low Fe contents are expected in the authigenic phases composing modern microbialites, which usually form in well oxygenated and alkaline water, because of the low solubility of Fe under these conditions (Schwertmann, 1991). Nevertheless, some modern shallow-water microbialites from the alkaline Mexican Lakes Alchichica, Atexcac and La Preciosa have been recently reported to contain relatively high amounts of Fe, i.e. >0.44 wt.%

of Fe<sub>2</sub>O<sub>3</sub> (Kaźmierczak et al., 2011; Zeyen et al., 2015). In order to understand the origin of this enrichment in Fe and determine whether this is due to authigenesis or detrital input, we characterized the speciation of Fe in Lake Alchichica and Atexcac microbialites as well as in microbialites from three other distinct alkaline lakes located in the trans Mexican volcanic belt. For this purpose, we combined bulk x-ray diffraction, Fourier-transform infrared spectroscopy and x-ray absorption near-edge structure (XANES) spectroscopy analyses, coupled with scanning and transmission electron microscopies as well as x-ray microscopy analyses. Overall, this enabled us to develop a consistent assessment of the Fe-bearing mineral phases composing these diverse modern microbialites, and thereby infer some of the geochemical processes that give rise to Fe enrichments in microbialites.

## 2. MATERIALS AND METHODS

### 2.1. Samples

#### 2.1.1 Microbialite samples

Field campaigns were conducted in June 2007, January 2012 and May 2014. Seven samples of modern microbialites were collected in five lakes: Alchichica, La Preciosa, Atexcac, La Alberca de Los Espinos and Pátzcuaro, all located within the trans Mexican volcanic belt (TMVB), a continental volcanic arc with an East-West orientation (Ferrari et al., 2012). Lake Pátzcuaro is older than 30,000 years and is a lava-dammed basin (Israde-Alcántara et al., 2005). The other lakes are maar lakes formed by phreato-magmatic explosions during the Pleistocene (Armienta et al., 2008; Siebe et al., 2014). Atexcac, La Preciosa and Alchichica maars are composed of tuff rings (Carrasco-Núñez et al., 2007). La Alberca de Los Espinos maar is a tuff cone (Siebe et al., 2014). Table 1 summarizes the main physical and geochemical parameters of these lakes.

Lake Alchichica harbored a high density of microbialites forming meter-scale bioherms all around the lake (Fig. SI-1a and d). The carbonate mineralogy and microbial diversity of Lake Alchichica microbialites have been extensively studied (Każmierczak et al., 2011; Couradeau et al., 2011; Couradeau et al., 2013; Gérard et al., 2013; Saghaï et al., 2015; Saghaï et al., 2016). Many microbialites were white in cross-section, but some had a darker, orange to brown color as reported by Kaźmierczak et al. (2011). These orange-brown microbialites were located on the West shore of the lake (Fig. SI-1a). There, the crater rim was particularly steep due to the outcrop of a basaltic scoria cone (Fig. SI-1b). In the present study, we investigated Fe speciation in one sample of a brown, living (i.e. underwater and covered by a biofilm) microbialite sampled in May 2014 on the West shore of Lake Alchichica (AL2014-15) (Fig. SI-1c), and two white, living microbialites from the North shore, collected in June 2007 at a depth of about 0.1 and 4 meters and named AL13 and AL66, respectively (Fig. SI-1e).

Microbialites from Lake La Preciosa and Lake Atexcac were described by Zeyen et al. (2015). Fossil (i.e. dry and not covered by a biofilm) microbialites formed steep bioherms on the North shore of Lake La Preciosa (Fig. SI-1f). A grey fossil microbialite (Preciosa05-2012) was analyzed in the present study (Fig. SI-1g). Microbialites from Lake Atexcac formed a steep wall superimposed on the crater walls (Fig. SI-1h). Here, a living microbialite showing a grey to orange color inside (ATX-2C1-2012) was sampled on the northern wall of the lake (Fig. SI-1i). Lake La Alberca de Los Espinos harbored decimeter-sized living microbialites restricted to a small area close to the West shore of the lake. Here, the studied sample contained some black small columns and orange pustules (AlbEsp2014-01) (Fig. SI-1j and k). Finally, living microbialites were collected on the north-eastern shore of Lake Pátzcuaro. Here, we studied a decimeter-sized brownish living laminated stromatolite (Patz2014-02), encrusting a basaltic rock (Fig. SI-1l and m). To our knowledge, microbialites from Lake

Pátzcuaro and Lake La Alberca de Los Espinos have not been reported before.

### 2.1.2. Synthetic model compounds

#### *Syntheses of nanocrystalline Fe(II):talc and Fe(III):talc*

Talc model compounds containing Fe(II) or Fe(III), partially substituted for Mg, referred to as nano-Fe(II):talc and nano-Fe(III):talc respectively, were synthesized using the protocol described by Juillot et al. (2006), with the stoichiometry  $\text{Fe}_{0.05}\text{Mg}_{2.95}\text{Si}_4\text{O}_{10}(\text{OH})_2$ , close to that measured by electron microprobe in Atexcac microbialites (Zeyen et al., 2015). For this purpose, a solution of 200 ml of sodium metasilicate  $\text{Na}_2\text{SiO}_3 \cdot 5\text{H}_2\text{O}$  (0.1 M) was prepared. Then, for the synthesis of nano-Fe(III):talc, a mixture of  $\text{Fe(III)Cl}_3 \cdot 6\text{H}_2\text{O}$  (0.01 M) and  $\text{MgCl}_2 \cdot 6\text{H}_2\text{O}$  (0.29 M) was homogenized. Fifty milliliters of the Fe/Mg mixture were added to 200 ml of the sodium meta-silicate solution. After this step, the pH of the solution was 11.4. The pH was adjusted to around 10.9 using HCl (1M) and the solution was homogenized for 30 minutes. Precipitates were centrifuged at 9000 g for 10 minutes and washed four times with milli-Q water before being transferred into 8 glass serum bottles sealed with a butyl rubber stopper and an aluminum cap (0.5 g of hydrated precipitate per flask), each containing 100 ml of water. Flasks were placed in an oven for 7 days at 80°C. Finally, the solutions were centrifuged at 9000 g for 10 minutes and washed four times with milli-Q water. Precipitates were dried in the desiccator overnight. For the synthesis of nano-Fe(II):talc, the same protocol as above was followed except that the synthesis was carried out in an anaerobic glove box using  $\text{O}_2$ -free milli-Q water, and  $\text{FeCl}_2 \cdot 4\text{H}_2\text{O}$  was used as a Fe(II) source. For this synthesis, the precipitate obtained before the aging period at 80°C was also washed and dried, and is designed hereafter as nano-Fe(II):talc-gel. In addition, in order to mimic oxidation of the structural Fe(II) in talc, a sample of nano-Fe(II):talc-gel dry powder was oxidized in an excess of 1 ml of 3%  $\text{H}_2\text{O}_2$  for about 5 hours before being rinsed with

milli-Q water and air dried. The resulting sample was referred to as nano-Fe(II):talc-gel H<sub>2</sub>O<sub>2</sub> oxidized.

### *Synthesis of Fe(III):hydrotalcite*

Hydrotalcite containing Fe(III) as impurity, referred to as Fe(III):hydrotalcite, was synthesized with the following stoichiometry: Mg<sub>0.75</sub>Al<sub>0.24</sub>Fe(III)<sub>0.01</sub>OH<sub>2</sub>(CO<sub>3</sub>)<sub>0.125</sub>. For this purpose, a 100 mL solution containing MgCl<sub>2</sub>·6H<sub>2</sub>O (0.06 M), Al<sub>2</sub>(SO<sub>4</sub>)<sub>3</sub>·18H<sub>2</sub>O (0.01 M) and Fe(III)Cl<sub>3</sub>·6H<sub>2</sub>O (0.0008 M) was titrated with a mixture of NaOH (1.6 M) and Na<sub>2</sub>CO<sub>3</sub> (0.1 M) to pH 10. The solution was stirred for one hour. The precipitate was then centrifuged four times at 9000 g for 10 minutes and rinsed with milli-Q water. Finally, the precipitate was placed in a desiccator overnight. The purity of the synthesized phases was checked by FTIR and/or XRD (Fig. SI-2).

## **2.2 Methods**

A quantity of about 10 g for each microbialite sample was finely ground in an agate mortar and aliquots of the same powdered sample were used for the different bulk analyses.

### **2.2.1. Bulk chemical analyses of microbialites**

Bulk chemical compositions of microbialite samples were determined by the *Service d'Analyse des Roches et Minéraux* (SARM, Centre de Recherches Pétrographiques et Géochimiques, Nancy, France). About 2 g of ground powders were used for these analyses. Major element analyses were performed using an ICP-AES ICap 6500 (Thermo Fischer) after alkali fusion of rock samples with LiBO<sub>2</sub> followed by dissolution in HNO<sub>3</sub>. The uncertainties of the major element measurements were between 1% and 25% depending on their

concentrations (Table 2).

### **2.2.2. Bulk mineralogical analyses of microbialites**

#### *X-ray diffraction (XRD)*

The bulk mineralogical composition of microbialites was determined by XRD. About 1 g of each microbialite powder was deposited on an aluminum sample holder. XRD measurements were performed using a Panalytical X'Pert diffractometer equipped with a cobalt anode (Co-K $\alpha$ ). Data were recorded at 40 kV and 40 mA in continuous-scan mode between 5 and 90° (2 $\theta$ ) with a step of 0.008°/s and a total counting time of ~3 h per scan. XRD data were analyzed using the PANalytical X'Pert Highscore software for background subtraction, peak finding, and matching with XRD patterns of reference compounds from the International Crystal Structure Database (ICSD, Fachinformationszentrum Karlsruhe, Germany; US Institute of Standards and Technology, USA).

#### *Fourier transform infrared (FTIR) spectroscopy*

For FTIR spectroscopy analyses, 2.5 mg of microbialite powder and 300 mg of potassium bromide (KBr) were mixed and ground in an agate mortar. A KBr pellet was prepared for each microbialite sample using a vacuum press under 8 tons for 1 minute. Pellets were placed overnight in an oven (95°C) to remove the adsorbed water and were pressed a second time. Transmission spectra were recorded as 210 replicate scans between 400 and 4000 cm<sup>-1</sup> with 1 cm<sup>-1</sup> resolution, using a Nicolet 6700 FTIR spectrometer.

### **2.2.3. Analyses of bulk Fe speciation by x-ray absorption near-edge structure (XANES) spectroscopy**

X-ray absorption near-edge structure (XANES) data of 7 microbialite samples (AL66, AL13, AL2014-15, Preciosa05-2012, ATX-2C1-2012, AbEsp2014-01 and Patz2014-02) were collected at the Fe K-edge in the fluorescence detection mode on beamline BM23 at the ESRF (Grenoble, France) using a Si(111) double crystal monochromator and a 13 elements Ge array detector. Duplicate data were recorded for sample AL66 on beamline BM30B FAME at the ESRF (Grenoble, France) using a Si(220) double crystal monochromator with sagittal focusing of the second crystal, and a 30 elements Ge array detector. Sample pellets were prepared using 130-230 mg of powder for all samples but the AL2014-15 sample, for which 5 mg of powder were mixed with 50 mg of cellulose. In addition, XANES spectra were collected for 3 model compounds: Fe(III):hydrotalcite, nano-Fe(II):talc and nano-Fe(III):talc. This was achieved in transmission detection mode at the BM23 beamline on pellets prepared by mixing 20-30 mg sample with 40-30 mg cellulose. Analyses were conducted at a temperature of ~10 K. Energy was calibrated by setting to 7112 eV the first inflection point of the Fe K-edge XANES spectrum of a reference Fe(0) foil, recorded simultaneously with the samples. For each microbialite sample and model compound, 2–8 scans were recorded, depending on the Fe concentration. XANES spectra were acquired from a range of 7000–7575 eV. The background Fe fluorescence signal arising from the excitation of the beamline components by diffuse scattering (e.g. sample chamber inner walls and Fe impurities in Be windows) was collected by measuring a XANES spectrum on a pure cellulose pellet. All data were averaged and normalized using the ATHENA software (Ravel and Newville, 2005).

Fe K-edge XANES spectra of the microbialite samples were analyzed using a linear combination least-squares fitting (LC-LSF) procedure that was performed with a custom-built software based on a Levenberg–Marquardt least-squares minimization algorithm (Hohmann et al., 2011; Stetten et al. 2017). A large set of already available Fe K-edge XANES spectra of

natural and synthetic model compounds was already available for this fitting procedure. This dataset included a large variety of synthetic Fe compounds such as Fe(III) (oxyhydr)oxides, e.g. goethite ( $\alpha$ -FeOOH) and 6-line ferrihydrite (Maillot et al., 2011; Hohmann et al., 2011) and siderite ( $\text{FeCO}_3$ ) (Dublet et al., 2014), and 2) natural phyllosilicates (Cosmidis et al., 2014; Othmane et al., 2013), such as serpentine from New Idria Mining District (CA, USA) (Dublet et al., 2012; Noël et al., 2014) and illite from Le Puy-en-Velay, France, i.e.,  $\text{Na}_{0.01}\text{K}_{0.64}\text{Ca}_{0.06}(\text{Al}_{1.19}\text{Fe(III)}_{0.36}\text{Mg}_{0.43}\text{Ti}_{0.04}\text{Mn}_{0.01})(\text{Si}_{3.53}\text{Al}_{0.47})\text{O}_{10}(\text{OH})_2$  (Ildefonse et al., 1998). This latter model compound, referred to as Fe(III):illite hereafter, was used as a proxy for structural Fe(III) in a dioctahedral 2:1 phyllosilicate. The background Fe signal from the beamline was systematically included as an additional component in the XANES LC-LSF procedure and accounted for 1 to 28% of the measured signal (Table SI-1), depending on Fe concentration and the amount of analysed microbialite sample. The quality of the LCF fits was estimated by a reduced chi-square parameter  $\chi^2_{\text{R}} = n / (n-p) \sum [\mu_{\text{exp}} - \mu_{\text{calc}}]^2$  where  $n$  is the number of independent parameters corresponding to the energy range divided by the natural width of the Fe K levels reported by Krause and Oliver (1979). The uncertainty on the fitting components was estimated by  $3 \times \sqrt{\text{VAR}(p) \chi_{\text{R}}^2}$ , where  $\text{VAR}(p)$  is the variance of parameter  $p$  returned by the Levenberg–Marquardt routine for the lowest  $\chi^2_{\text{R}}$  value (Stetten et al., 2017).

#### 2.2.4. Microscopy analyses of microbialites

##### *Sample preparation for microscopy analyses*

Some microbialite samples (ATX-2C1-2012, Preciosa05-2012 and AlbEsp2014-01) were sawed to obtain ~5 mm thick sections and polished down to a ¼ of micron of surface roughness with diamond polishing compounds. Then, they were rinsed in an ultrasonic



cleaning bath with pure ethanol. Finally, polished sections were dried overnight in a desiccator. Samples were mounted on 2.5 cm wide aluminum stubs using double-sided carbon tape. Alchichica and Pátzcuaro microbialite samples (AL13, AL66, AL2014-15 and Patz-2014-02) were dehydrated in a gradual series of ethanol baths (30%, 50%, 70%, 90% and 100%), and progressively impregnated with hard grade LR-white resin (Polysciences, Inc.). The samples were incubated for 18 h at 4-6°C in 1:2 (1:1 for AL13 and AL66 samples) and then in 2:1 mixture of LR-white/ethanol, and finally in pure LR-white resin. After 3 h at room temperature, samples were embedded in pure LRwhite resin for 1 h at 40°C and then for 24 h at 60°C. After polymerization, transverses sections were cut with a diamond wire to obtain ~2 mm thick sections and polished until 1/4 µm of surface roughness. All samples were carbon-coated, except AlbEst2014-01, which was platinum-coated.

#### *Scanning electron microscopy (SEM)*

Scanning electron microscopy analyses were performed using a Zeiss ultra 55 field emission gun (FEG) SEM. Backscattered electron (BSE) images were acquired using an angle selective backscattered (AsB) detector at an accelerating voltage of 15 kV and a working distance of ~7.5 mm. The elemental composition of mineral phases was determined by energy dispersive x-ray spectrometry (EDXS) using an EDS QUANTAX detector. EDXS data were analyzed using the ESPRIT software package (Bruker).

#### *Micro x-ray fluorescence (µXRF) mapping*

X-ray fluorescence images were collected on AL13 and AL66 microbialite samples at the Stanford synchrotron radiation lightsource (SSRL) using beam line 2–3. The incident energy was set to 11 keV using a Si (111) double crystal monochromator with the storage ring Stanford Positron Electron Accelerating Ring (SPEAR) containing 500 mA in top-off mode at

3.0 GeV. The fluorescence lines of the elements of interest, as well as the intensity of the total scattered X-rays, were monitored using a Si drift Vortex detector (SII NanoTechnology USA Inc.) equipped with Xspress3 pulse processing electronics (Quantum Detectors). The raw spectra were binned at the time of collection into regions of interest representing the peak areas of the fluorescence emission. The entire fluorescence spectrum was also collected at each data point. The microfocused beam of 2x2 $\mu$ m was provided by a Pt-coated Kirkpatrick-Baez mirror pair (Xradia Inc.). The incident and transmitted x-ray intensities were measured with nitrogen-filled ion chambers. Samples were mounted at 45° to the incident x-ray beam and were spatially rastered in the microbeam using a Newport VP-25XA-XYZ stage. Beam exposure was 50 ms per pixel. Image data was processed using the MicroAnalysis Toolkit (Webb, 2011). The fluorescence regions of interest were corrected for any variations in the incident beam intensity, and placed on the same absolute magnitude scale for each individual element (Fe, Ca) for comparison between samples.

#### *Focused ion beam (FIB) sectioning*

Four ultrathin electron-transparent foils were cut from polished sections AL13, AL66, AL2014-15 and ATX-2C1-2012 by focused ion beam milling using a FEI Strata Dual-beam 235 instrument operating at 30 kV and 5 nA following the FIB lift-out method as described by Benzerara et al. (2005). Before milling, a platinum strap was deposited onto the region of interest of the sample. After *in situ* transfer to a copper grid, the foil was thinned down to around 100 nm with a Ga<sup>+</sup> beam current of about 100 pA and at glancing angle.

#### *Transmission electron microscopy (TEM)*

FIB foils were analyzed by a JEOL 2100F transmission electron microscope (TEM) operating at 200 kV. This microscope is equipped with a FEG, an ultra-high resolution pole

piece, a Gatan energy filter GIF 2001, a JEOL detector with an ultrathin windowing detection of light elements, and a scanning TEM (STEM) device, which allows Z-contrast imaging in high angle annular dark field (HAADF) mode. Elemental mapping was acquired by EDXS in the STEM mode, using the JEOL software Analysis Station. Selected area electron diffraction (SAED) patterns were recorded to identify mineral phases and assess their crystallinity. SAED patterns were processed using the Image J software in order to measure *d*-spacings. The Crystallmaker software was used to index diffraction patterns.

### *Scanning transmission x-ray microscopy (STXM)*

FIB foils extracted from Alchichica (AL13 and AL66) and Atexcac (ATX-2C1-2012) microbialite samples were analyzed by STXM at the C K-edge and the Fe L<sub>2,3</sub>-edges. Analyses were performed on beamline 11.0.2.2 at the Advanced Light Source (Berkeley, USA), using a 25 nm zone plate. Energy calibration was achieved using the well-resolved 3p Rydberg peak of gaseous CO<sub>2</sub> at 294.96 eV. Data included image stacks, from which XANES spectra and maps were retrieved. The aXis2000 software (Hitchcock, 2012) was used for data processing. More details on the principles of STXM can be found in Bourdelle et al. (2013).

## **3. RESULTS**

### **3.1. Bulk chemical composition of Mexican microbialites**

Microbialites from the different lakes showed diverse Fe contents (Table 2). Fe content in the microbialites from Preciosa05-2012 (Lake La Preciosa), AlbEsp2014-01 (Lake La Alberca de Los Espinos), ATX-2C1-2012 (Lake Atexcac), and Patz2014-02 (Lake Pátzcuaro) ranged between  $0.31 \pm 0.02$  wt.% and  $0.62 \pm 0.03$  wt.%. In Lake Alchichica, the white microbialites from the North shore (AL13) had a low Fe content of  $0.12 \pm 0.01$  wt.%, whereas the brown microbialites from the West shore (AL2014-15) contained a much higher

Fe content of  $2.24 \pm 0.04$  wt.%.

While Al and K contents correlated positively together (Fig. SI-3a), no correlation was detected between the Fe content and the Al, K or Ti contents of microbialites (Fig. SI-3b-c-d). For example, sample AL2014-15 had the highest Fe content but a Ti content below the detection limit (Table 2, Fig. SI-3d). This suggested that Fe was predominantly carried by non-detrital phases

### 3.2. Fe bulk speciation in Mexican microbialites

In order to obtain further insight on the identity of the mineral phases hosting Fe, XANES spectroscopy measurements were conducted at the Fe K-edge. These analyses were complemented by XRD and FTIR analyses for mineral identification. Altogether, these analyses showed that Fe-speciation in Alchichica microbialites (AL13, AL66 and AL2014-15) clearly differed from that in the other lakes.

#### 3.2.1. Speciation of Fe in microbialites from Lake Alchichica

Our best LC-LSF results for the Fe K-edge XANES spectra of all the Alchichica microbialites (AL2014-15, AL66 and AL13) were obtained by including a significant to major Fe(III):hydrotalcite component in the fits (Figs. 1 and SI-4; Tables 3 and SI-1), up to 100% in the AL66 spectrum. This component was interpreted here as a proxy for Fe(III)-bearing layered double hydroxide (LDH), i.e., an anionic clay, with the general stoichiometry  $[M(II)_{1-x}M(III)_x(OH)_2][A^{n-}_{x/n}] \cdot mH_2O$ , where M(II) (e.g., Mg(II)) and M(III) (e.g., Fe(III)) are di- and tri-valent cations in the octahedral sites within the hydroxide layers and  $A^{n-}$  (e.g.,  $Cl^-$  or  $CO_3^{2-}$ ) is an exchangeable interlayer anion (Mills et al., 2012). Goethite and ferrihydrite fitting components were also found in the AL2014-15 spectrum, while nano-Fe(II):talc was needed to fit the AL13 spectrum. The nano-Fe(II):talc component was considered as a proxy

for Fe(II) in a trioctahedral 2:1 phyllosilicate structure. These XANES results indicated that AL2014-15 and AL66 microbialites contained Fe as Fe(III) only, whereas around 30% of Fe in AL13 microbialite was in the form of Fe(II).

FTIR and XRD analyses showed that AL13 and AL66 microbialites were mainly composed of hydromagnesite ( $\text{Mg}_5(\text{CO}_3)_4(\text{OH})_2 \cdot 4\text{H}_2\text{O}$ ) with lower amounts of aragonite ( $\text{CaCO}_3$ ), whereas AL2014-15 was mostly composed of aragonite with lower amounts of hydromagnesite (Figs. 2 and 3). In agreement with XANES analyses, the weak peaks at 7.59 Å ( $13.4^\circ 2\theta$ ) and 3.79 Å ( $27.3^\circ 2\theta$ ) in the XRD pattern of the Fe-rich AL2014-15 sample (2.23 wt.%; Table 3) were consistent with the (003) and (006) Bragg reflections of LDH, respectively (Fig. 2). Accordingly, a peak at  $1384\text{ cm}^{-1}$  was also detected in the same sample by FTIR spectroscopy (Fig. 3a) and could be interpreted as the carbonate asymmetric stretching mode ( $\nu_3\text{CO}_3$ ) in LDH (Ross et Kodama, 1967; Braithwaite et al., 1994; Frost and Erickson, 2004), indicating the presence of a  $\text{CO}_3$ -containing LDH phase. This peak has been also detected in aragonite by Jones and Jackson (1993), although we did not observe it in the aragonite sample from Molina, Aragon, Spain in the RRUFF database (RRUFF ID: R040078; data not shown). The  $\nu_3\text{CO}_3$  FTIR peak at  $1384\text{--}1385\text{ cm}^{-1}$  possibly indicative of LDH (e.g., pyroaurite and/or iowaite) was also detected in the Fe-poor AL13 and AL66 sample as a faint shoulder of an intense band attributed to hydromagnesite (Fig. 3c). LDH was not detected by XRD in these samples (Fig. 2), which could be explained by the very low Fe contents in these samples (e.g. 0.13 wt.% in AL13; Table 2). No peak at  $\sim 3680\text{ cm}^{-1}$ , indicative of  $\text{Mg}_3\text{-OH}$  stretching bands, characteristic of Mg in octahedral coordination such as in kerolite (Tosca et al., 2011), was observed for sample AL13. Moreover, such a phase was not detected by XRD in this sample, suggesting that if present, it was only in minute amount. The (101) Bragg reflection at 4.18 Å (e.g.,  $24.7^\circ 2\theta$ ) of goethite (Schwertmann and Cornell, 2000) was not detected by XRD in AL2014-15, possibly because of overlap with the aragonite and

hydromagnesite patterns. Ferrihydrite could not be detected by XRD possibly owing to its nanocrystalline structure (Table 2).

### **3.2.2. Speciation of Fe in microbialites from Lakes La Preciosa, Atexcac, La Alberca de Los Espinos and Pátzcuaro**

The Fe K-edge XANES spectra of microbialites from La Preciosa, Atexcac, La Alberca de Los Espinos and Pátzcuaro were all best fitted with a combination of Fe:clay components, namely nano-Fe(II): and/or nano-Fe(III):talc and Fe(III):illite (Figs. 4 and SI-4; Tables 3 and SI-1). Linear fits with other model compounds, such as 1:1 phyllosilicate model compound (e.g., serpentine), provided lower quality fits. The nano-Fe(II):talc fitting component was considered as a proxy for Fe(II) substituting for Mg(II) in the octahedral layer of a trioctahedral 2:1 phyllosilicate, which was confirmed by a shell-by-shell analysis of this model compound (Materials and methods SI-1; Fig. SI-5; Table SI-2). Besides, the local structure around Fe in the synthetic nano-Fe(III):talc fitting component was close to that in the nano-Fe(II):talc-gel oxidized by H<sub>2</sub>O<sub>2</sub> and considered as a proxy for the poorly ordered oxidation byproduct of nano-Fe(II):talc (Figs. SI-5 and SI-6). The Fe K-edge EXAFS spectra of these Fe(III)-bearing talc model compounds significantly differed from those of ferrihydrite and illite (Fig. SI-6), indicating different local structures around Fe(III) in these three compounds (Table SI-2). Moreover, these three compounds could also be well distinguished by XANES as shown in Figs. 1 and 4. Fe(III):illite was considered as a proxy for Fe(III) in the octahedral layer of a dioctahedral 2:1 phyllosilicate in the LC-LSF XANES analysis of the microbialite samples. A large fraction of Fe (69-73%) was present in a nanocrystalline trioctahedral 2:1 phyllosilicate in the Preciosa05-2012 and ATX-2C1-2012 samples with 22-26% of total Fe as Fe(II). The nanocrystalline trioctahedral 2:1 phyllosilicate

fraction was slightly lower in the AlbEsp201-01 (57%) and Patz2014-02 (67%) samples as well as the Fe(II) to total Fe proportion (9-10% of total Fe) (Tables 3 and SI-1).

Bulk XRD analyses showed that the major mineral phases composing these microbialites were: aragonite and calcite in La Preciosa; aragonite, calcite and hydromagnesite in Atexcac; calcite and monohydrocalcite in La Alberca de Los Espinos; calcite, monohydrocalcite and aragonite in Pátzcuaro (Fig. 5). In addition, broad peaks at 4.5 Å ( $22.8^\circ$   $2\Theta$ ), 2.5 Å ( $42.3^\circ$   $2\Theta$ ) and 1.5 Å ( $72.1^\circ$   $2\Theta$ ) were detected in XRD patterns of Preciosa05-2012, ATX-2C1-2012 and Patz2014-02. These peaks may correspond to *d*-spacings at 4.55, 2.48 and 1.52 Å corresponding to two dimensional *hk* diffraction bands (respectively (02-11), (13-20) and (06-33)) characteristic of poorly ordered layer silicate such as hydrated talc (kerolite) or trioctahedral smectite phases (stevensite) (Brindley et al., 1955; Brindley et al., 1977) and/or dioctahedral Fe-smectite such as nontronite (Decarreau et al., 2008). Moreover, faint shoulders at  $\sim 11$  Å ( $9.3^\circ$   $2\Theta$ ) and  $\sim 10$  Å ( $10^\circ$   $2\Theta$ ) in the XRD patterns of the Preciosa05-2012 and Patz2014-02 samples, could correspond to basal reflections of poorly ordered smectite and talc phases, respectively (Fig. 5). The near absence of the (001) reflection could be consistent with a strong phase disorder and/or with the presence of nanophases(s). Some kerolite/stevensite/nontronite was also present in AlbEsp2014-01 as shown by a faint peak at 4.5 Å ( $22.8^\circ$   $2\Theta$ ) (Inset Fig. 5). In contrast, XRD patterns were not suggestive of 1:1 silicates (e.g., serpentine). For example, the (001) peak of lizardite (RRUFF ID: R060006) or antigorite (RRUFF ID: R070228) at 7.27 Å was not observed. Consistently, FTIR spectra of all four microbialites showed one peak at 1020-1026  $\text{cm}^{-1}$  (Fig. 6a), interpreted as Si-O stretching in tetrahedral vibration in a 2:1 layered configuration of tetrahedral silicate layers and octahedral  $\text{MgO}_6$  layers. This is consistent, but not exclusively, with the presence of a kerolite and/or stevensite phase. However, this large band at 1020-1026  $\text{cm}^{-1}$  is not observed in 1:1 layered configuration silicates such as serpentines, which are

mainly characterized by 2 bands around 990 et 1080  $\text{cm}^{-1}$  (Yariv and Heller-Kallai, 1975). FTIR spectra of all four microbialites also showed one peak at 3679-3681  $\text{cm}^{-1}$ , interpreted as a  $\text{Mg}_3\text{-OH}$  stretching band, characteristic of Mg in octahedral coordination, consistent but not exclusively with kerolite/stevensite (Fig. 6b; Tosca et al., 2011). Additional bands at 3624 and 3647  $\text{cm}^{-1}$  in the Pátzcuaro microbialite may result from a splitting of the hydroxyl stretching in kerolite due to the substitution of Mg by Fe (Fig. 6b; Wilkins and Ito, 1967). Again, these bands are significantly different from those observed in 1:1 layered configuration silicates such as serpentines, which appear at 3652, 3669, 3688 and 3703  $\text{cm}^{-1}$  for lizardite (Trittschack et al., 2012) or 3644 and 3689  $\text{cm}^{-1}$  in chrysotile (Bishop et al., 2002). Last but not least, the  $\nu_3\text{CO}_3$  band at 1384-1385  $\text{cm}^{-1}$  was detected in La Preciosa, Atexcac, La Alberca de Los Espinos and Pátzcuaro (Fig. 6 a-c). While this band may be due to LDH and/or aragonite in ATX-2C1-2012, Preciosa05-2012, and Patz2014-02, it was likely associated with LDH in AlbEsp2014-02 since no other band characteristics of aragonite was observed in this sample.

### 3.3. Microscopy analyses of Fe-bearing phases

Fe-rich areas were observed by microscopy in all the samples except the La Preciosa microbialite. Light and scanning electron microscopies as well as  $\mu\text{-XRF}$  analyses showed that Fe distribution in microbialites was discrete, with the existence of Fe-hotspots (Figs. 7 and 8). In AL2014-15, Fe was contained in numerous thin laminae, measuring less than 10  $\mu\text{m}$  in thickness as well as patches of  $\sim 100$   $\mu\text{m}$  in width (Fig. 7 a-b). Fe-rich phases sometimes appeared extinct under cross polars as observed for AL2014-15 suggesting the presence of a poorly crystalline phase. In AL13, Fe hotspots appeared as laminae and patches beneath an aragonite layer located at the surface of microbialites (Fig. 7 c-d). In ATX-2C1-2012 and Patz2014-02, Fe phases were distributed as  $\sim 50\text{-}200$   $\mu\text{m}$  thick laminae (Fig. 7 e-f-g-h).



### 3.3.1. Fe-bearing phases in Alchichica microbialites

Synchrotron-based  $\mu$ -XRF maps showed that Fe in AL66 was concentrated in discrete laminae, beneath an aragonite layer located at the surface of microbialites (Fig. 8 a-b). The same Fe-rich areas were analyzed at a higher spatial resolution by SEM-EDXS. These Fe laminae showed a smooth texture and were sandwiched between a surface layer of aragonite and an inner mass of hydromagnesite (Fig. 8). One FIB foil was cut across a Fe-rich lamina (Fig. 8c) and analyzed by TEM. At the nanoscale, one phase with a fibrous texture appeared to bear Fe together with Mg and Cl and almost no Al (Fig. 9 a-b-e area#1). The selected area electron diffraction (SAED) pattern of this phase showed diffuse spots with  $d$ -spacings at 2.65, 2.43 and 1.55 Å corresponding to the (101), (0-11) and (-1-10) lattice planes, respectively, viewed along the [1-1-1] zone axis of a LDH phase (Fig. 9c). In accordance with bulk XAS analyses, this phase was interpreted as a Mg-, Fe-, and Cl-rich LDH phase, i.e. iowaite ( $\text{Mg}_6\text{Fe(III)}_2(\text{OH})_{16}\text{Cl}_2 \cdot 4\text{H}_2\text{O}$ ). Iowaite was overlain by crystalline micritic aragonite as attested by EDXS and SAED analyses (Figs. 9 a-b-d-e area#2 and SI-7).

Similar as in AL66, Fe-rich areas in AL13 also appeared between a surface aragonite layer and an inner mass of hydromagnesite forming the bulk of the microbialite (Fig. 10). Some Fe-rich laminae were also detected within the aragonite layer and a FIB foil was cut across one of them (Fig. 10c). The Fe-rich lamina sampled in the FIB foil measured  $\sim 1 \mu\text{m}$  in width. It was smooth and darker than the surrounding aragonite by STEM-HAADF (Fig. 11). This lamina was mostly composed of Mg, Cl and Fe, similarly to iowaite in AL66 with minor amounts of Si and Al. However, the rings in the SAED pattern were much more diffuse so that  $d$ -spacings could not be determined (Fig. 11d). Fe in this phase was mostly in the form of Fe(III) as shown by the prominent peak at 710.3 eV in the XANES spectrum measured by STXM at the Fe  $L_{2,3}$ -edges (Fig. 11g). This agreed with bulk XAS measurements. Finally, this

Fe-rich lamina contained organic matter as attested by STXM analyses at the C K-edge (Fig. 11 h-i). Indeed, XANES spectra measured on the lamina showed peaks at 1) 284.9 eV, interpreted as carbon  $1s \rightarrow \pi^*$  electronic transitions in aromatic and/or olefinic groups ( $C=C$ ); 2) 286.6 eV, interpreted as carbon  $1s \rightarrow \pi^*$  electronic transitions in ketone/phenol group ( $C=O$ ); 3) 287.3 eV, interpreted as carbon  $1s \rightarrow \sigma^*$  transitions in aliphatic groups and 4) 288.5 eV, interpreted as carbon  $1s \rightarrow \pi^*$  transitions in carboxylic functional groups (Fig. 11i, Benzerara et al., 2004; Bernard et al., 2010). An additional peak at 290.3 eV was interpreted as carbonate C (Benzerara et al., 2004), suggesting that in addition to iowaite, there was also a  $CO_3$ -containing LDH phase, i.e. pyroaurite ( $Mg_6Fe(III)_2(OH)_{16}CO_3 \cdot 4H_2O$ ), in accordance with FTIR analyses.

AL2014-15 contained a much higher Fe content than AL13 and AL66. Consistently, large Fe-rich areas were observed by light microscopy and SEM (Figs. 7 a-b and 12). A FIB foil was cut within one of these areas, across two Mg- and Fe-rich, Si-poor objects with circular cross-sections surrounded by a Fe- and Si-rich mineral matrix (Fig. 12). TEM analyses showed three different mineral phases with different textures in the FIB foil (Fig. 13): 1) pyroaurite/iowaite, appearing smooth when observed by bright-field TEM and STEM-HAADF and forming bands measuring 200 nm to 1  $\mu m$  in width and filling partially the objects. This phase was composed of Mg, Cl and Fe and showed a SAED pattern consistent with pyroaurite/iowaite observed along the  $[1-1-1]$  zone axis (Fig. 13a-b-c area#1-d). 2) The second mineral phase was fibrous and corresponded to the matrix surrounding the objects (Fig. 13 a-b-f-g). This phase was composed of Fe with Si and Mg as shown by EDXS analyses with a Fe proportion ( $X_{Fe}=Fe/(Mg+Fe)$ ) close to 0.7 (Fig. 13 c area#2). Its SAED pattern showed diffuse rings at  $\sim 3.15$ ,  $\sim 2.55$  and  $\sim 1.50$  Å (Fig. 13 a-e), consistent with phyllosilicates such as the silico-ferric precipitates synthesized at 150°C by Decarreau et al. (1987). The  $d$ -spacings at 2.55 and 1.50 Å were also compatible with the (110) and (300)

planes of ferrihydrite, that may contain high amount of Si (Schwertmann and Cornell, 2000).  
3) Aragonite appeared as well crystalline micrometer-sized grains in bright-field TEM (Fig. 13 f-h).

### **3.3.2. Fe-bearing phases in Atexcac, La Alberca de Los Espinos and Pátzcuaro microbialites**

Although Fe contents in ATX-2C1-2012, Patz2014-02 and AlbEsp2014-01 were relatively low, some Fe-containing areas could be detected by SEM-EDXS (Fig. 14). In all of them, Fe was systematically associated with Si and Mg (Fig. 14), consistently with bulk XAS, FTIR and XRD analyses that showed Fe incorporation in a talc-like phase. The presence of Fe in a talc-like phase in ATX-2C1-2012 microbialite sample was also supported by previous electron microprobe analyses showing (Mg+Fe)/Si ratio equal to  $0.82 \pm 0.06$  (Zeyen et al., 2015). Moreover, most of the occurrences that we observed were Al-poor except for Patz2014-02 (Fig. 14 d-e-f). FIB foils were cut within two distinct Fe-rich areas in ATX-2C1-2012: one was analyzed by Zeyen et al. (2015); one has been characterized by TEM and STXM in the present study (Figs. 15 and 16). This FIB foil contained two mineral phases: 1) aragonite which appeared as aggregated crystalline grains measuring few hundreds of nanometers, with a high diffraction contrast in bright field TEM, and a bright contrast in STEM-HAADF; 2) the Fe-rich phase with a smooth texture and a darker contrast in STEM-HAADF (Fig. 15 c-d). SAED patterns acquired on the Fe-rich phase showed very diffuse rings attesting that it was poorly crystalline (Fig. 15e). In agreement with SEM observations, STEM-EDXS analyses indicated that this Fe-rich phase contained mostly Si and Mg (Fig. 15h). Some Al was also detected here in contrast with SEM analyses and previous TEM analyses on Fe- and Mg-rich silicates reported by Zeyen et al. (2015). XANES spectroscopy at the Fe  $L_{2,3}$ -edges indicated that Fe was mostly in the form of Fe(III) in this phase (Fig. 16 a-b). Again, this Fe- and Si-rich phase was associated with organic matter. XANES spectrum

at the C K-edge showed the same peaks as observed in the AL13 iowaite/pyroaurite lamina, indicative of aromatic and/or olefinic, ketone/phenol, aliphatic and carboxylic C-functional groups (Fig. 16c). Similarly, a peak located at 290.4 eV was observed and could be interpreted as carbonate C and/or metal-carboxylic C complexes (Chan et al., 2009).

## 4. DISCUSSION

### 4.1. Origins of the Fe content in Mexican microbialites: authigenesis vs detrital input

The Fe content of Mexican microbialites varied between 0.12 wt.% in AL13 and 2.24 wt.% in AL2014-15. Depending on the lakes, Fe was found in a variety of mineral phases as summarized in Table 4, including pyroaurite/iowaite, Fe-bearing kerolite/stevensite, a dioctahedral 2:1 phyllosilicate, possibly illite and/or a smectite phase such as nontronite, ferrihydrite and possibly goethite, as inferred by a combination of XANES, XRD, FTIR and electron microscopy. As a comparison, carbonates (specifically analyzed by leaching experiments) within modern marine microbialites from the Heron Reef Formation (Australia) contained lower Fe concentrations, less than 0.005 wt.% (Von Blanckenbourg et al., 2008). The chemically sorted carbonate fraction composing Archaean stromatolites studied by Von Blanckenbourg et al. (2008) from the Strelley Pool Formation (Pilbara craton, Australia), the Mushandike Formation (Masvingo Greenstone Belt, Zimbabwe craton), the Gamohaan, Kogelbeen and the Boomplaas formations (Kaapvaal craton, South Africa) had Fe concentrations ranging from 0.02 to 1.51 wt.%. Proterozoic stromatolites from the 1.89 Ga Gunflint and Biwabik Fe formations (Animikie basin) studied by Planavsky et al. (2009) had Fe contents varying between 0.02 and 14.11 wt.%, with Fe possibly comprised within hematite, magnetite, siderite and/or ankerite as inferred by XRD and standard petrographic techniques. All of them were interpreted as microbially-mediated authigenic phases. Overall,

Fe contents of the modern Mexican microbialites appeared relatively high, considering that they formed at shallow depth in oxic and alkaline water. Carbonate phases were a negligible carrier of Fe in Mexican microbialites. Instead, Fe was found in discrete laminae between distinct carbonate phases, such as hydromagnesite and aragonite. This suggests that Mexican microbialites formed by alternating periods when Fe-poor carbonates formed and periods when Fe-rich phases formed. Moreover, in Alchichica microbialites, Fe-rich laminae outlined some transition between hydromagnesite and aragonite laminae. Such an association is difficult to explain based on the hypothesis made by Kaźmierczak et al. (2011), who proposed that hydromagnesite forms secondarily as a replacement of aragonite. In contrast, the Holocene hydromagnesite deposits at Atlin (British Columbia, Canada) are mainly composed of hydromagnesite and magnesite, while aragonite is only observed in crack fills suggesting a primary origin for hydromagnesite formed by both abiotic and biotic processes (Stamatakis et al. 2007). In the Kozani Basin, an ancient lacustrine system in Greece, Stamatakis (1995) showed that  $p\text{CO}_2$  was the key parameter explaining the precipitation of hydromagnesite versus huntite, aragonite and brucite. Similarly, the aragonite-pyroaurite/iowaite-hydromagnesite association in Lake Alchichica may result from some significant hydrochemical variations, which occurred at a certain time in the lake from conditions conducive to hydromagnesite precipitation to conditions favoring aragonite formation through an episode of pyroaurite/iowaite precipitation. Regardless, we note that the environmental message carried by Fe in these microbialites relates to the origin and the fate of oxyhydroxides, silicates and layered double hydroxides and not the carbonate phases (i.e. aragonite, hydromagnesite, calcite or monohydrocalcite).

Some of the Fe-bearing phases may be detrital. In AL13, Preciosa05-2012, ATX-2C1-2012, AlbEsp2014-02 and Patz2014-02, XANES spectra included the contribution of a Fe-bearing dioctahedral 2:1 phyllosilicate. While the XANES spectrum of illite was used a

reference endmember for the fitting procedure, no illite was detected by XRD. Instead, this Fe-bearing dioctahedral 2:1 phyllosilicate might be nontronite, consistent with XRD data measured on Preciosa05-2012 and Patz2014-02 samples (Decarreau et al., 2008). Moreover, the occurrence within microbialites of nontronite, a common alteration product of basalt, would be consistent with the alteration of the surrounding mafic catchment/bedrock (Velde, 2003). Alternatively, the broad XRD peaks at 4.5, 2.5 and 1.5 Å may relate to Mg-kerolite and/or stevensite only and not Fe-bearing phases. Microscopy analyses showed some occurrences of mineral phases containing Mg, Fe, Si and Al in ATX-2C1-2012 and Patz2014-02, which could be nontronite. Nevertheless, it should be noticed that a Mg-, Fe- and Si-rich phase with a very similar texture and no Al was also found in ATX-2C1-2012 (Zeyen et al., 2015), suggesting that if a dioctahedral 2:1 phyllosilicate such as nontronite phase may contain some of the Fe, an Al-free phyllosilicate also accommodates some of the Fe. Whatever the identity of the Fe-carrying dioctahedral 2:1 phyllosilicate, several observations suggest that a significant amount of Fe was carried by non-detrital phases in Mexican microbialites. First, no correlation was observed between Fe and the Al, K and Ti bulk contents of the microbialites, as this would be expected from a major detrital input. Moreover, Fe-bearing phases observed by microscopy frequently displayed textures indicative of *in situ* precipitation such as Fe-bearing phases templating objects with circular cross-sections, possibly biogenic structures. Thus, authigenesis scenarios are provided hereafter for the formation of Fe-bearing kerolite/stevensite-like and pyroaurite/iowaite phases, two of the main Fe-bearing phases detected in the microbialites.

#### **4.2. Fe-bearing layered double hydroxides in Alchichica microbialites**

In Alchichica microbialites, part and sometimes most of Fe was borne by layered double hydroxides (LDH), sometimes referred to as hydrotalcite (Hall and Stamatakis, 2000),

a mineral supergroup comprising more than 40 naturally-occurring mineral species with a layered double hydroxide structure (Mills et al., 2012). LDH structure consists of positively charged brucite-type layers ( $\text{Mg}(\text{OH})_2$ ) separated by intercalated, charge balancing anions (Schutz and Biloen, 1987). Chemical compositions of LDH widely vary (Allada et al., 2006) in terms of their divalent cation content (e.g.,  $\text{Mn}(\text{II})$ ,  $\text{Mg}(\text{II})$ ,  $\text{Ni}(\text{II})$ ), their trivalent cation content (e.g.,  $\text{Al}(\text{III})$ ,  $\text{Fe}(\text{III})$ ,  $\text{Cr}(\text{III})$ ) and the interlayer anions (e.g.,  $\text{CO}_3^{2-}$ ,  $\text{NO}_3^-$ ,  $\text{Cl}^-$ ,  $\text{SO}_4^{2-}$ ). Here, XANES, FTIR, STXM and TEM analyses showed that the LDH phase in Alchichica microbialites contained chloride and carbonates as interlayer anions, Mg as a divalent cation and Fe(III) as a trivalent cation. Therefore, this phase belongs to the iowaite ( $\text{Mg}_6\text{Fe}(\text{III})_2(\text{OH})_{16}\text{Cl}_2 \cdot 4\text{H}_2\text{O}$ ) – pyroaurite ( $\text{Mg}_6\text{Fe}(\text{III})_2(\text{OH})_{16}\text{CO}_3 \cdot 4\text{H}_2\text{O}$ ) group.

A carbonate-bearing LDH phase was also detected by FTIR in microbialites from La Preciosa, Atexcac, La Alberca de Los Espinos and Pátzcuaro. However, XAS and electron microscopy analyses suggested that this phase was not a significant carrier of Fe in these microbialites, either because this phase was hydrotalcite *sensu stricto*, i.e. it contained Al(III) instead of Fe(III) as a trivalent cation and/or because iowaite/pyroaurite was rare compared to other Fe-phases.

Iowaite was first described in Precambrian serpentinites (Kohls and Roda, 1967). Nonetheless, this alteration phase postdates the formation and its age is not known. Iowaite and pyroaurite are rare minerals but they have been found in abundance in ultramafic deposits (e.g., Kohls and Rodda, 1967; Frost and Erickson, 2004; Bach et al., 2004; Turvey et al., 2017). For example, pyroaurite has been detected as one of the weathering byproducts of serpentinite following infiltration of alkaline ( $\text{pH} > 8$ ) groundwater rich in  $\text{Mg}^{2+}$ ,  $\text{HCO}_3^-$ ,  $\text{SO}_4^{2-}$  and  $\text{Cl}^-$  (Taylor et al., 1991; Milodowski et al., 2009; Stamatakis and Mitsis, 2013). Pyroaurite is supposed to be late-stage alteration phase forming under oxidizing conditions (Bach et al., 2004). However, based on laboratory experiments, McCollom et al. (2016) suggested that

iowaite may precipitate under reducing conditions in some cases. Interestingly, the same mineral assemblage as that observed in Alchichica microbialites, i.e. pyroaurite and/or iowaite together with hydromagnesite, has been classically detected in carbonation products of the ultramafic tailings of the Clinton Creek asbestos mine (Yukon, Canada), the Mount Keith nickel mines (Western Australia) and the Woodsreef tailings (New South Wales, Australia) (Wilson et al., 2014; Power et al., 2014, McCutcheon et al., 2016; Turvey et al., 2017). Moreover, hydrotalcite, manasseite ( $\text{Mg}_6\text{Al}_2(\text{CO}_3)(\text{OH})_{16}\cdot 4\text{H}_2\text{O}$ ) and pyroaurite were observed in close association with hydromagnesite in heavily sheared serpentinized rocks in Nain Ophiolites (Iran) (Eslami et al., 2015). These authors argued that these Mg- and Fe-rich carbonates were formed by the percolation of Mg-rich meteoric water through serpentinites. Similarly, pyroaurite in association with hydromagnesite have also been observed as secondary alteration byproducts of serpentinites in the ophiolites from the Geraneia Mountains (Greece) due to groundwater circulation of alkaline fluids with a high Mg/Ca ratio (Stamatakis and Mitsis, 2013). Last, LDH (including iowaite) have been highlighted in a context of active serpentinization in hyperalkaline springs in Oman (Chavagnac et al., 2013). Nevertheless, the geodynamic environment in Alchichica is very different, indicating that the paragenesis hydromagnesite/pyroaurite-iowaite can be found in other environments than ultramafic massifs. Indeed, no ultramafic deposit has ever been reported in Alchichica or within the broader Serdan-Oriental Basin, where deposits are invariably basaltic, andesitic or rhyolitic (e.g., Siebe et al., 1995; Zimmer et al., 2010; López-Rojas and Carrasco-Nunez, 2015). On the West shore of Lake Alchichica, where we observed the largest LDH contents in microbialites, the nearby basaltic scoria cone is the most likely Fe-rich source explaining the local high enrichment of microbialites in Fe. The high alkalinity of Lake Alchichica, possibly due to microbial activity, together with its low concentration in dissolved  $\text{H}_4\text{SiO}_4$ , possibly due to diatom activity, may explain why overall Lake Alchichica hydrochemistry looks



similar to that of fluids in weathered ultramafic settings and therefore why precipitating mineral phases are similar to those found in these environments.

In the context of basalt alteration, LDH phases can also form, but in this case the trivalent cation is generally Al(III). The mineral phase hydrotalcite ( $\text{Mg}_6\text{Al}_2(\text{OH})_{16}\text{CO}_3 \cdot 4\text{H}_2\text{O}$ ) was observed in several experiments altering basalt glass in seawater (Larsen et al., 1991; Thomassin and Touray, 1982; Crovisier et al., 1983a; Abdelouas et al., 1994). For example, basaltic glass experimentally altered at 50°C for 20 days was shown to be covered by a layered alteration shell, comprising hydrotalcite between an inner serpentine-type phyllosilicate layer and a saponite layer (Crovisier et al., 1983a). However, it was reported that pyroaurite formed at a lower temperature of 25°C after 240 days (Crovisier et al., 1983b). The authors suggested that hydrotalcite formed at 50°C, because at this temperature Fe was poorly mobile and stayed at the base of the alteration shell, while at 25°C, Fe was more mobile and could react with dissolved Mg to precipitate pyroaurite from the solution. The absence of Al in Alchichica LDH phases suggests that they were not formed at the contact of basalts before transport to the microbialites but more likely formed from a solution similar to that prevailing in experiments by Crovisier et al. (1983b).

Whatever the geodynamic context, several modes of pyroaurite/iowaite formation have been suggested: these phases can form through a solid-state transformation of Fe(II)-bearing brucite by oxidation of Fe(II) to Fe(III) accompanied by the  $\text{Cl}^-$  and  $\text{CO}_3^{2-}$  incorporation between brucite layers (Heling and Schwarz, 1992). Alternatively, Grguric et al. (2001) proposed that iowaite and pyroaurite formed by transformation of magnetite by reaction with alkaline and Cl-rich brines in the Mount Keith nickel deposits. Similarly, Wang et al. (2013) showed the transformation of lepidocrocite and akaganeite into iowaite after their exposure to the salt aerosols of Lake Qinghai. Last, Hansen and Koch (1995) showed that pyroaurite can precipitate from solution following Fe(II) oxidation in Mg-rich, carbonate-

705 and/or  $\text{Cl}^-$ -containing solutions at  $\text{pH} > 8.5$ . Here, we have no definitive evidence allowing us  
706 to discriminate between these three possibilities for the formation of pyroaurite/iowaite in  
707 Lake Alchichica. Nonetheless, in some cases, we observed that iowaite/pyroaurite was  
708 contained in biomorphs and was associated with organic matter down to the nm-scale (Figs.  
709 11 and 13), suggesting that it may have precipitated from solution in contact with  
710 microorganisms. Metagenomic studies of Lake Alchichica microbialites did not evidence 16S  
711 rDNA gene sequences indicative of classically known Fe-cycling bacteria, i.e., dissimilatory  
712 Fe-reducing bacteria or Fe-oxidizing bacteria (Saghaï et al., 2015 and 2016). However, these  
713 studies have shown that microbialites are associated with a large proportion of photosynthetic  
714 microorganisms that need Fe as a nutrient. Interestingly, there were significant differences in  
715 the local diversity of photosynthetic eukaryotes associated with North vs West microbialites.  
716 While diatoms dominated the eukaryotic fraction of a microbialite sample from the seepage-  
717 influenced West shore of Lake Alchichica, they were marginal in North shore microbialites,  
718 where eukaryotes were scarce and dominated by green algae (Saghaï et al., 2015 and 2016).  
719 In our study, the microbialite sample from the West shore of Lake Alchichica showed a  
720 higher Si concentration ( $1.02 \pm 0.05$  wt.%) compared to the microbialite from the North shore  
721 ( $0.65 \pm 0.03$  wt.%) (Table 2) and was characterized by large areas of Si associated with Fe  
722 (Fig. 12). This Si likely came from the groundwater seepage, which has been shown to be  
723 more Si-rich (between 13 and 230 times higher) than the Lake Alchichica water (Table 1;,  
724 Armienta et al., 2008; Kaźmierczak et al., 2011; Sigala et al., 2017). Future studies  
725 documenting the relative contribution of hydrothermalism/underground water to the  
726 hydrological budget of the lake will be interesting to address this point. The existence of local  
727 seepage rich in  $\text{H}_4\text{SiO}_4$  on the West shore is also consistent with the local proliferation of  
728 diatoms. In turn, diatom abundance implies the increased in situ availability of Si in  
729 microbialites from frustule dissolution. Therefore, in addition to the local variation of water

chemistry, the differential composition of microbial communities could also explain, at a smaller scale, the different type of minerals observed within microbialites. Microbes could play an important role in the precipitation of Fe-bearing phases by influencing particular concentration of ions (such as Fe or Si). Furthermore, the patchy distribution of Fe in microbialites suggests that Fe-rich conditions might be locally and temporally limited. Finding living microbialites mineralizing under Fe-rich conditions would be useful in order to better understand the potential interactions existing between microorganisms and Fe, their involvement in Fe-rich phase formation and subsequent transformation.

Overall, we suggest the following scenario similar to that proposed by Taylor et al. (1991) for the formation of pyroaurite associated with the weathering of partially serpentinised harzburgite in Oman (Fig. 17): (1) basalts around Lake Alchichica, outcropping mostly on the West shore of the lake, were altered by the circulation of groundwater anoxic fluids. Fe(II) but little Al and Si were released into these fluids. (2) When these fluids came into contact with Lake Alchichica water, Fe(II) became oxidized in a  $\text{Cl}^-$ ,  $\text{Mg}^{2+}$ ,  $\text{CO}_3^{2-}$  and  $\text{O}_2$ -rich solution as well as at high pH (~9) and high alkalinity (~40 mM), favoring pyroaurite/iowaite precipitation. Alternatively, Fe(II) may oxidize and be sequestered as Fe-oxyhydroxides first before secondary transformation into pyroaurite/iowaite following prolonged contact with Lake Alchichica water. Noteworthy, Fe-oxyhydroxides phases such as ferrihydrite have a slightly higher solubility at pH=9 than at pH=7 (Stefánsson, 2007). In addition, the presence of organic molecules may also increase the apparent solubility of Fe by complexation (Kuma et al., 1996), making Fe available for pyroaurite precipitation. Overall, the high Fe content in the microbialites and the presence of iowaite/pyroaurite trace groundwater input to the formation of microbialites.

#### **4.3. LDH vs silicates**

While iowaite/pyroaurite were major carriers of Fe in Alchichica microbialites, these phases were not observed in microbialites from other lakes. Poorly crystalline Fe-bearing talc-like phases were observed instead. An authigenic hydrated and poorly crystalline talc-like phase ( $\text{Mg}_3\text{Si}_4\text{O}_{10}(\text{OH})_2 \cdot n\text{H}_2\text{O}$ ) similar to kerolite and/or stevensite was detected in Lake Atexcac by Zeyen et al. (2015). Lake Atexcac, Lake La Preciosa, Lake Patzcuaro and Lake La Alberca de Los Espinos were all shown to be supersaturated with regards to Mg-silicates (Zeyen et al., 2017), which supports the possibility that such a phase precipitates in these lakes. Moreover, it was shown by microscopy that this phase sometimes contains Fe in Lake Atexcac, in agreement with the possibility that Fe(II) substitutes for Mg(II) and Fe(III) substitutes for Mg(II) (with the loss of a proton) and/or Si in the structure of nanocrystalline 2:1 trioctahedral phyllosilicates such as kerolite and/or stevensite (Forbes, 1969; Corona et al., 2015).

It is important to note that the majority of Fe was in the form of Fe(III) in all Mexican microbialites. Fe may have been incorporated as Fe(II) in kerolite and/or stevensite before later solid-state oxidation at the contact with oxic water. This is consistent with the fact that EXAFS results on our model compounds suggest that the nano-Fe(III):talc component identified in the XANES spectrum of the Preciosa05-2012, AlbEsp2014-01, ATX-2C1-2012 and Patz2014-02 microbialite samples can be interpreted as a byproduct of the oxidation of a nano-Fe(II)-talc component (Fig. SI-5). In the present study, we extend the record of such Fe-bearing talc phases to Lake La Alberca de Los Espinos and Lake Pátzcuaro. Following what was observed in Lake Alchichica, we proposed that Fe-enrichments may also be due to seepage in these volcanic lakes bringing Fe(II)-rich fluids to oxic water.

The reason why Fe was incorporated into pyroaurite/iowaite in Lake Alchichica vs kerolite/stevensite in other lakes, despite similar total Fe contents, might be related to the differences in chemical conditions prevailing in these lakes. Although the formation of

pyroaurite/hydrotalcite may require relatively higher pH than a silicate phase (e.g., Besson et al., 1974; Miyata and Okada, 1977; Crovisier et al., 1983b), this may not be a major parameter here since all studied lakes had similar pH values 8.5-9 (Zeyen et al., 2017). In contrast,  $\text{H}_4\text{SiO}_4$  concentrations were much lower in Lake Alchichica ( $[\text{H}_4\text{SiO}_4] = 0.017 \text{ mM}$ ; Kaźmierczak et al., 2011) compared to the other lakes which showed orthosilicic acid concentrations higher than 0.37 mM and up to 1.0 mM in Lake Atexcac (Zeyen et al., 2015 & 2017). Chavagnac et al. (2013) argued that the chemical composition of the solution, specifically its  $\text{H}_4\text{SiO}_4$  concentration, is of essential importance in controlling the type of clay (cationic or anionic) formed. These authors detected LDH, including iowaite, in a springwater with a low  $\text{H}_4\text{SiO}_4$  content ( $<10 \text{ }\mu\text{M}$ ) and a high pH (12). Interestingly, previous experimental studies of basaltic glass alteration have shown that hydrotalcite can transform into an Al-bearing serpentine and/or a smectite-like Fe-Mg-rich phase following reaction of the hydrotalcite precursor with orthosilicic acid accumulating at an increasing concentration in the solution (Thomassin and Touray, 1982; Crovisier et al., 1983a; Abdelouas et al., 1994). This hydrotalcite to silicate transformation has been suggested to occur through dissolution/precipitation in the presence of dissolved orthosilicic acid (Besson et al. 1974). Overall, LDH may form and stay preserved in Lake Alchichica because of the low  $[\text{H}_4\text{SiO}_4]$  prevailing in this lake, while in other lakes, Fe-bearing kerolite or smectite phases form from the transformation of a transient iowaite/pyroaurite phase or direct precipitation. Future synthesis experiments will be necessary to better constrain chemical parameters (e.g.,  $[\text{H}_4\text{SiO}_4]$ , alkalinity) favoring silicates versus LDH-like phases within microbialites.

## 5. CONCLUSION

Microbialites from Mexican alkaline crater lakes sometimes contain high Fe contents.

A large part of Fe is in the form of Fe(III). Part of Fe is mineralized in authigenic phases, i.e. iowaite/pyroaurite in Lake Alchichica and Fe-bearing kerolite and/or stevensite in lakes La Preciosa, Atexcac, Pátzcuaro and La Alberca de Los Espinos. These Fe-bearing phases are distributed along discrete thin laminae as well as large Fe-rich areas within microbialites.

The concentration of orthosilicic acid in the lakes seems to be a major parameter controlling the nature of the Fe-bearing phases that form. To our knowledge, layered double hydroxide (LDH) phases such as iowaite/pyroaurite phases have never been reported before in ancient or modern microbialites. This might be due to 1) the specific chemical conditions required for their formation, e.g. high alkalinity,  $[\text{CO}_3^{2-}]$ , pH,  $[\text{Cl}^-]$  and  $[\text{Mg}^{2+}]$  combined with low  $[\text{H}_4\text{SiO}_4]$ ; 2) the difficulty in detecting and characterizing these phases, especially when there are in low abundance; 3) the reactivity of these phases to silica, leading to potentially poor preservation in the geological record; 4) the presence of specific microbial communities locally modifying ion concentrations and pH.

While the Fe-bearing phases in modern microbialites may carry some information on their formation conditions, their fate in the geological record remains unknown. In these Mexican lakes, the LDH phases appear to sometimes be finely associated with organic matter. How their formation and reactivity interfere with microbial communities populating the surface of these microbialites and to which extent these phases are implicated in the fossilization processes of microorganisms will deserve further attention. Furthermore, the precise range of geochemical conditions allowing pyroaurite-iowaite formation and the stability of LDH through geological time will need to be determined in the future. To our knowledge, no study exists on the fate and transformation of LDH over geological time. We postulate that aging not involving fluids may not modify drastically the mineralogy of these phases. However, late circulations of  $\text{H}_4\text{SiO}_4$ -rich fluids may transform LDH into phyllosilicates as shown by several studies (Crovisier, 1983a, Ford and Spark, 2000). If these

transformations keep textures intact, the present study offers textural examples of what should be looked for as remnants of LDH within ancient microbialites. In any case, the present study highlights the diversity of the mineral phases bearing Fe in modern environments. This calls for a careful reappraisal of the primary Fe-bearing phases in ancient microbialites so that meaningful paleoenvironmental interpretations can be retrieved from e.g. Fe isotope measurements.

## ACKNOWLEDGEMENTS

The research leading to these results has received funding from the European Research Council under the European Union's Seven Framework Program: ERC grants Calcyan (P.I.: K. Benzerara, Grant Agreement no. 307110) and ProtistWorld (P.I.: P. López-García, Grant Agreement no. 322669). The TEM facility at IMPMC was purchased through the support of Region Ile-de-France grant SESAME 2000 E 1435. The SEM facility at IMPMC was supported by Région Ile de France grant SESAME 2006 I-07-593/R. Advanced Light Source (ALS) Molecular Environmental Science beamline 11.0.2 is supported by the Office of Science, Office of Basic Energy Sciences, Division of Chemical Sciences, Geosciences, and Biosciences and Materials Sciences Division, U.S. Department of Energy, at the Lawrence Berkeley National Laboratory. Use of the Stanford Synchrotron Radiation Lightsource, SLAC National Accelerator Laboratory, is supported by the U.S. Department of Energy, Office of Science, Office of Basic Energy Sciences under Contract No. DE-AC02-76SF00515. The SSRL Structural Molecular Biology Program is supported by the DOE Office of Biological and Environmental Research, and by the National Institutes of Health, National Institute of General Medical Sciences (including P41GM103393). The contents of this publication are solely the responsibility of the authors and do not necessarily represent the

official views of NIGMS or NIH. We are indebted to Olivier Mathon for the setup of the BM23 beamline and for his help during data collection. We thank Ludovic Delbès and Benoît Baptiste for their technical support during XRD analyses and Agnès Elmaleh for valuable feedbacks on the manuscript.

## REFERENCES

- Abdelouas A., Crovisier J. L., Lutze W., Fritz B., Mosser A. and Mueller R. (1994) Formation of hydrotalcite-like compounds during R7T7 nuclear waste glass and basaltic glass alteration. *Clays and Clay Minerals* **42**, 526–533.
- Allada R. K., Peltier E., Navrotsky A., Casey W. H., Johnson C. A., Berbeco H. T. and Sparks D. L. (2006) Calorimetric determination of the enthalpies of formation of hydrotalcite-like solids and their use in the geochemical modeling of metals in natural waters. *Clays and Clay Minerals* **54**, 409–417.
- Armienta M. A., Vilaclara G., De la Cruz-Reyna S., Ramos S., Cenicerros N., Cruz O., Aguayo A. and Arcega-Cabrera F. (2008) Water chemistry of lakes related to active and inactive Mexican volcanoes. *Journal of Volcanology and Geothermal Research* **178**, 249–258.
- Bach W., Garrido C. J., Paulick H., Harvey J. and Rosner M. (2004) Seawater-peridotite interactions: First insights from ODP Leg 209, MAR 15°N. *Geochem. Geophys. Geosyst.* **5**, Q09F26.
- Benzerara K., Yoon T. H., Tyliczszak T., Constantz B., Spormann A. M. and Brown G. E. (2004) Scanning transmission X-ray microscopy study of microbial calcification. *Geobiology* **2**, 249–259.
- Benzerara K., Menguy N., Guyot F., Vanni C. and Gillet P. (2005) TEM study of a silicate-carbonate-microbe interface prepared by focused ion beam milling. *Geochim. Cosmochim. Acta* **69**, 1413–1422.
- Bernard S., Benzerara K., Beyssac O. and Brown G. E. (2010) Multiscale characterization of pyritized plant tissues in blueschist facies metamorphic rocks. *Geochim. Cosmochim. Acta* **74**, 5054–5068.
- Besson H., Caillère S. and Hénin S. (1974) Conditions de formation de divers hydrocarbonates voisins de l’hydrotalcite. *Bulletin du Groupe français des argiles* **26**, 79–90.
- Bishop J., Murad E. and Dyar M. D. (2002) The influence of octahedral and tetrahedral cation substitution on the structure of smectites and serpentines as observed through infrared spectroscopy. *Clay Minerals* **37**, 617–628.
- Bosak T., Knoll A. H. and Petroff A. P. (2013) The meaning of stromatolites. *Annual Review of Earth and Planetary Sciences* **41**, 21–44.
- Bourdelle F., Benzerara K., Beyssac O., Cosmidis J., Neuville D. R., Brown G. E. and Paineau E. (2013) Quantification of the ferric/ferrous iron ratio in silicates by scanning transmission X-ray microscopy at the Fe L<sub>2,3</sub>-edges. *Contributions to Mineralogy and Petrology* **166**, 423–434.
- Braithwaite R. S. W. (1994) Iowaite, a re-investigation. *Mineralogical Magazine* **58**, 79–85.



- 898 Brindley G. (1955) Stevensite, a montmorillonite-type mineral showing mixed-layer  
899 characteristics. *Am. Miner.* **40**, 239–247.
- 900 Brindley G. W. (1977) The nature of kerolite, its relation to talc and stevensite. *Mineralogical*  
901 *Magazine* **41**, 443–452.
- 902 Burne R.V., Moore L.S. (1987) Microbialites: organosedimentary deposits of benthic  
903 microbial communities. *Palaios* **2**, 241–254.
- 904 Carrasco-Núñez G., Ort M. H. and Romero C. (2007) Evolution and hydrological conditions  
905 of a maar volcano (Atexcac crater, Eastern Mexico). *Journal of Volcanology and*  
906 *Geothermal Research* **159**, 179–197.
- 907 Chagas A. A. P., Webb G. E., Burne R. V. and Southam G. (2016) Modern lacustrine  
908 microbialites: Towards a synthesis of aqueous and carbonate geochemistry and  
909 mineralogy. *Earth-Science Reviews* **162**, 338–363.
- 910 Chan C. S., Fakra S. C., Edwards D. C., Emerson D. and Banfield J. F. (2009) Iron  
911 oxyhydroxide mineralization on microbial extracellular polysaccharides. *Geochim.*  
912 *Cosmochim. Acta* **73**, 3807–3818.
- 913 Chavagnac V., Ceuleneer G., Monnin C., Lansac B., Hoareau G. and Boulart C. (2013)  
914 Mineralogical assemblages forming at hyperalkaline warm springs hosted on  
915 ultramafic rocks: A case study of Oman and Ligurian ophiolites. *Geochemistry,*  
916 *Geophysics, Geosystems* **14**, 2474–2495.
- 917 Cornelis P. (2014) Iron uptake and homeostasis in prokaryotic microorganisms. In *Binding,*  
918 *Transport and Storage of metal ions in biological cells* (eds. W. Maret and A. Wedd).  
919 Royal Soc. Chemistry, Cambridge.
- 920 Corona J. C., Jenkins D. M. and Dyar M. D. (2015) The experimental incorporation of Fe into  
921 talc: a study using X-ray diffraction, Fourier transform infrared spectroscopy, and  
922 Mössbauer spectroscopy. *Contributions to Mineralogy and Petrology* **170**.
- 923 Cosmidis J., Benzerara K., Morin G., Busigny V., Lebeau O., Jézéquel D., Noël V., Dublet G.  
924 and Othmane G. (2014) Biomineralization of mixed valence iron-phosphates in the  
925 anoxic water column of lake pavin (Massif Central, France). *Geochim. Cosmochim.*  
926 *Acta* **126**, 78–96.
- 927 Couradeau E., Benzerara K., Moreira D., Gérard E., Kaźmierczak J., Tavera R. and López-  
928 García P. (2011) Prokaryotic and eukaryotic community structure in field and cultured  
929 microbialites from the alkaline Lake Alchichica (Mexico) ed. J. A. Gilbert. *PLoS ONE*  
930 **6**, e28767.
- 931 Couradeau E., Benzerara K., Gérard E., Estève I., Moreira D., Tavera R. and López-García P.  
932 (2013) Cyanobacterial calcification in modern microbialites at the submicrometer  
933 scale. *Biogeosciences* **10**, 5255–5266.
- 934 Crovisier J. L., Thomassin J. H., Juteau T., Eberhart J. P., Touray J. C. and Baillif P. (1983a)  
935 Experimental seawater-basaltic glass interaction at 50°C: Study of early developed  
936 phases by electron microscopy and X-ray photoelectron spectrometry. *Geochim.*  
937 *Cosmochim. Acta* **47**, 377–387.
- 938 Crovisier J., Ehret G., Pierre Eberhart J. and Juteau T. (1983b) Altération expérimentale de  
939 verre basaltique tholeiitique par l'eau de mer entre 3 et 50°C. *Sci. Géol., Bull,*  
940 *Strasbourg* **36**, 187–206.
- 941 Decarreau A., Bonnin D., Badaut-Trauth D., Couty R. and Kaiser P. (1987) Synthesis and  
942 crystallogenesis of ferric smectite by evolution of Si-Fe coprecipitates in oxidizing  
943 conditions. *Clay Minerals* **22**, 207–223.
- 944 Decarreau A., Petit S., Martin F., Farges F., Vieillard P. and Joussein E. (2008) Hydrothermal  
945 synthesis, between 75 and 150 °C, of high-charge, ferric nontronites. *Clays and Clay*  
946 *Minerals* **56**, 322–337.
- 947 Dublet G., Juillot F., Morin G., Fritsch E., Fandeur D., Ona-Nguema G., Brown Jr. G.E.

- (2012) Ni speciation in a New Caledonian lateritic regolith: A quantitative X-ray absorption spectroscopy investigation. *Geochim. Cosmochim. Acta* **95**, 119–133.
- Dublet G., Juillot F., Morin G., Fritsch E., Noël V., Brest J. and Gordon G. E. (2014) XAS evidence for Ni sequestration by siderite in a lateritic Ni-deposit from New Caledonia. *Am. Miner.* **99**, 225–234.
- Eslami A., Stamatakis M. G., Perraki M., Vasilatos C. and Hollingbery L. (2015) On the occurrence of Mg- and Fe-rich carbonate mineral assemblages hosted in the Nain ophiolite mélange, Central Iran and their industrial potential. *Neues Jahrbuch für Mineralogie - Abhandlungen Journal of Mineralogy and Geochemistry* **192**, 59–71.
- Ferrari L., Orozco-Esquivel T., Manea V. and Manea M. (2012) The dynamic history of the Trans-Mexican Volcanic Belt and the Mexico subduction zone. *Tectonophysics* **522–523**, 122–149.
- Forbes W.C. (1969) Unit-cell parameters and optical properties of talc on the join  $\text{Mg}_3\text{Si}_4\text{O}_{10}(\text{OH})_2\text{--Fe}_3\text{Si}_4\text{O}_{10}(\text{OH})_2$ . *Am. Miner.* **5**, 1399–1408.
- Ford R. G. and Sparks D. L. (2000) The nature of Zn precipitates formed in the presence of pyrophyllite. *Environ. Sci. Technol.* **34**, 2479–2483.
- Frost R. L. and Erickson K. L. (2004) Vibrational spectroscopy of stichtite. *Spectrochimica Acta Part A: Molecular and Biomolecular Spectroscopy* **60**, 3001–3005.
- Gérard E., Ménez B., Couradeau E., Moreira D., Benzerara K., Tavera R. and López-García P. (2013) Specific carbonate–microbe interactions in the modern microbialites of Lake Alchichica (Mexico). *The ISME journal* **7**, 1997–2009.
- Grguric B. A., Madsen I. C. and Pring A. (2001) Woodallite, a new chromium analogue of iowaite from the Mount Keith nickel deposit, Western Australia. *Mineralogical Magazine* **65**, 427–435.
- Hall A. and Stamatakis M. G. (2000) Hydrotalcite and an amorphous clay mineral in high-magnesium mudstones from the Kozani Basin, Greece. *Journal of Sedimentary Research* **70**, 549–558.
- Hansen H. C. B. and Koch C. B. (1995) Synthesis and characterization of pyroaurite. *Applied clay science* **10**, 5–19.
- Heling D. and Schwarz A. (1992) Iowaite in serpentinite muds at Sites 778, 779, 780, and 784: a possible cause for the low chlorinity of pore waters. In *Proceedings of the Ocean Drilling Program, Scientific Results* (eds. P. Fryer, J.A. Pearce, L.B. Stokking et al.). Ocean Drilling Program College Station, TX, USA **125**, pp. 313–323.
- Hitchcock A. (2012) *aXis 2000 – Analysis of X-ray Images and Spectra*. Available at: <<http://unicorn.mcmaster.ca/aXis2000.html>> [accessed February 16, 2012].
- Hohmann C., Morin G., Ona-nguema G., Guigner J. M., Brown G. E. and Kappler A. (2011) Molecular-level modes of As binding to Fe (III) (oxyhydr)oxides precipitated by the anaerobic nitrate-reducing Fe(II)-oxidizing Acidovorax sp. Strain BoFeN1. *Geochim. Cosmochim. Acta* **75**(17), 4699–4712.
- Ildefonse Ph., Caberet D., Saintavit P., Calas G., Flank A.-M. and Lagarde P. (1998) Al X-ray absorption near edge structure in model compound and earth's surface minerals. *Phys. Chem. Minerals* **25**, 112–121.
- Israde-Alcántara I., Garduño-Monroy V. H., Fisher C. T., Pollard H. P. and Rodríguez-Pascua M. A. (2005) Lake level change, climate, and the impact of natural events: the role of seismic and volcanic events in the formation of the Lake Pátzcuaro Basin, Michoacan, Mexico. *Quaternary International* **135**, 35–46.
- Jones G. C. and Jackson B. (1993) *Infrared Transmission Spectra of Carbonate Minerals*. Springer Netherlands.
- Juillot F. (2006) EXAFS signature of structural Zn at trace levels in natural and synthetic trioctahedral 2:1 phyllosilicates. *Am. Miner.* **91**, 1432–1441.

- 998 Kamber B. S. and Webb G. E. (2007) Transition metal abundances in microbial carbonate: a  
999 pilot study based on in situ LA-ICP-MS analysis. *Geobiology* **5**, 375–389.
- 1000 Kaźmierczak J., Kempe S., Kremer B., López-García P., Moreira D. and Tavera R. (2011)  
1001 Hydrochemistry and microbialites of the alkaline crater lake Alchichica, Mexico.  
1002 *Facies* **57**, 543–570.
- 1003 Kohls D. and Rodda J. (1967) Iowaite a new hydrous magnesium hydroxide ferric  
1004 oxychloride from Precambrian of iowa. *Am. Miner.* **52**, 1261–1271.
- 1005 Krause M. O. and Oliver J. H. (1979) Natural widths of atomic K and L levels, K $\alpha$  X-ray  
1006 lines and several KLL Auger lines. *J. Phys. Chem. Ref. Data* **8**, 329–338.
- 1007 Kuma K., Nishioka J. and Matsunaga K. (1996) Controls on iron(III) hydroxide solubility in  
1008 seawater: The influence of pH and natural organic chelators. *Limnology and*  
1009 *Oceanography* **41**, 396–407.
- 1010 Larsen G., Plum K. H. and Förster H. (1991) Zeolites and other hydrothermal alteration  
1011 products of synthetic glasses. *Eur. J. Mineral.* **3**, 933–941.
- 1012 López-Rojas M. and Carrasco-Núñez G. (2015) Depositional facies and migration of the  
1013 eruptive loci for Atexcac axalapazco (central Mexico): implications for the  
1014 morphology of the crater. *Revista Mexicana de Ciencias Geológicas* **32**, 377–394.
- 1015 Maillot F., Morin G., Wang Y., Bonnin D., Ildefonse P., Chaneac C. and Calas G. (2011)  
1016 New insight into the structure of nanocrystalline ferrihydrite: EXAFS evidence for  
1017 tetrahedrally coordinated iron (III). *Geochim. Cosmochim. Acta* **75**(10), 2708–2720.
- 1018 McCollom T. M., Klein F., Robbins M., Moskowitz B., Berquo T. S., Joens N., Bach W. and  
1019 Templeton A. (2016) Temperature trends for reaction rates, hydrogen generation, and  
1020 partitioning of iron during experimental serpentinization of olivine. *Geochim.*  
1021 *Cosmochim. Acta* **181**, 175–200.
- 1022 McCutcheon J., Wilson S. A. and Southam G. (2016) Microbially Accelerated Carbonate  
1023 Mineral Precipitation as a Strategy for in Situ Carbon Sequestration and Rehabilitation  
1024 of Asbestos Mine Sites. *Environmental Science & Technology* **50**, 1419–1427.
- 1025 Mills S. J., Christy A. G., Génin J.-M. R., Kameda T. and Colombo F. (2012) Nomenclature  
1026 of the hydrotalcite supergroup: natural layered double hydroxides. *Mineralogical*  
1027 *Magazine* **76**, 1289–1336.
- 1028 Milodowski A. E., Constantinou C. A., Alexander W. R., Rigas M., Tweed C. J., Sellin P.,  
1029 Korkeakoski P., Kemp S. J. and Rushton J. C. (2009) Reaction of bentonite in low  
1030 alkali cement leachates: Preliminary results from the Cyprus Natural Analogue Project  
1031 (CNAP). Available at: <http://nora.nerc.ac.uk/id/eprint/9948> [Accessed June 19, 2017].
- 1032 Miyata S. and Okada A. (1977) Synthesis of hydrotalcite-like compounds and their physico-  
1033 chemical properties - the systems Mg<sup>2+</sup>-Al<sup>3+</sup>-SO<sub>4</sub><sup>2-</sup> and Mg<sup>2+</sup>-Al<sup>3+</sup>-CrO<sub>4</sub><sup>2-</sup>. *Clays and*  
1034 *Clay Minerals* **25**, 14–18.
- 1035 Noël V., Marchand C., Juillot F., Ona-Nguema G., Viollier E., Marakovic G., Olivi L., Delbes  
1036 L., Gelebart F., Morin G. (2014) EXAFS analysis of iron cycling in mangrove  
1037 sediments downstream of a lateritized ultramafic watershed (Vavouto Bay, New  
1038 Caledonia). *Geochim. Cosmochim. Acta* **136**, 211–228.
- 1039 Othmane G., Allard T., Morin G., Sélo M., Menguy N., Brest J. and Llorens I. (2013) Chen.  
1040 N., Bargar J. R., Fayek M., Calas G., Uranium association with iron-bearing phases in  
1041 milltailings from Gunnar, Canada. *Environ. Sci. Technol.* **47**(22), 12695–12702.
- 1042 Petrash D. A., Robbins L. J., Shapiro R. S., Mojzsis S. J. and Konhauser K. O. (2016)  
1043 Chemical and textural overprinting of ancient stromatolites: Timing, processes, and  
1044 implications for their use as paleoenvironmental proxies. *Precambrian Research* **278**,  
1045 145–160.
- 1046 Planavsky N., Rouxel O., Bekker A., Shapiro R., Fralick P. and Knudsen A. (2009) Iron-  
1047 oxidizing microbial ecosystems thrived in late Paleoproterozoic redox-stratified

- oceans. *Earth and Planetary Science Letters* **286**, 230–242.
- Power I., McCutcheon J., Harrison A., Wilson S., Dipple G., Kelly S., Southam C. and Southam G. (2014) Strategizing carbon-neutral mines: A Case for Pilot Projects. *Minerals* **4**, 399–436.
- Ravel B. and Newville M. (2005) Athena, Artemis, Hephaestus: data analysis for X-ray absorption spectroscopy using Ifeffit. *J. Synchrotron Radiat.* **12**, 537–541.
- Ross G. and Kodama H. (1967) Properties of a synthetic magnesium-aluminum carbonate hydroxide and its relationship to magnesium-aluminum double hydroxide manasseite and hydrotalcite. *Am. Miner.* **52**, 1036–1047.
- Saghai A., Zivanovic Y., Zeyen N., Moreira D., Benzerara K., Deschamps P., Bertolino P., Ragon M., Tavera R., López-Archilla A. I. and López-García P. (2015) Metagenome-based diversity analyses suggest a significant contribution of non-cyanobacterial lineages to carbonate precipitation in modern microbialites. *Frontiers in Microbiology* **6**.
- Saghai A., Zivanovic Y., Moreira D., Benzerara K., Bertolino P., Ragon M., Tavera R., López-Archilla A. I. and López-García P. (2016) Comparative metagenomics unveils functions and genome features of microbialite-associated communities along a depth gradient: Comparative metagenomics of microbialites from Lake Alchichica. *Environmental Microbiology* **18**, 4990–5004.
- Schutz A. and Biloen P. (1987) Interlamellar chemistry of hydrotalcites: I. Polymerization of silicate anions. *Journal of Solid State Chemistry* **68**, 360–368.
- Schwertmann U. (1991) Solubility and dissolution of iron oxides. *Plant Soil* **130**, 1–25.
- Schwertmann U. and Cornell R.M. (2000) *Iron oxides in the laboratory: Preparation and characterization*. Wiley-VCH, New York.
- Siebe C., Macias, Luis J., Abrams M., Rodriguez S., Castro R. and Delgado H. (1995) Quaternary explosive volcanism and pyroclastic deposits in east central Mexico: implications for future hazards. *Geological Society of America Annual Meeting, New Orleans, Louisiana*. 1–48.
- Siebe C., Guilbaud M.-N., Salinas S., Kshirsagar P., Chevrel M. O., de la Fuente J. R., Jiménez A.H. and Godinez L. (2014) Monogenetic volcanism of the Michoacán-Guanajuato Volcanic Field: Maar craters of the Zacapu basin and domes, shields, and scoria cones of the Tarascan highlands (Paracho-Paricutin region). In *Field guide, Pre-meeting Fieldtrip for the 5th International Maar Conference*, Querétaro, 13–17 November, México, 33 p.
- Sigala I., Caballero M., Correa-Metrio A., Lozano-García S., Vázquez G., Pérez L. and Zawisza E. (2017) Basic limnology of 30 continental waterbodies of the Transmexican Volcanic Belt across climatic and environmental gradients. *Boletín de la Sociedad Geológica Mexicana* **69**, 313–370.
- Stamatakis M. G. (1995) Occurrence and genesis of huntite hydromagnesite assemblages, Kozani, Greece –Important new white fillers and extenders. *Transactions of the institution of mining and metallurgy, section B applied Earth Science*, **104**, 179–186.
- Stamatakis M. G., Renaut R. W., Kostakis K., Tsivilis S., Stamatakis G. and Kakali G. (2007) The hydromagnesite deposits of the Atlin area, British Columbia, Canada, and their industrial potential as a fire retardant, *Bulletin of the Geological Society of Greece* **40**, 972.
- Stamatakis M. G. and Mitsis I. (2013) The occurrences of Mg-hydroxycarbonates in serpentinites of the western section of the South Aegean volcanic arc (West Attica peninsula-Northeastern Argolis peninsula), Greece. *Bulletin of the Geological Society of Greece, vol. XLVII 2013 Proceedings of the 13th International Congress, Chania, Sept. 2013* **47**, 427–437.

- 1098 Stetten L., Mangeret A., Brest J., Seder-Colomina M., Le Pape P., Ikogou M., Zeyen N.,  
1099 Thouvenot A., Julien A., Alcalde G., Reyss J.L., Bombled B., Rabouille C., Olivi L.,  
1100 Proux O., Cazala C., Morin G. (2017) Geochemical control on the reduction of U(VI)  
1101 to mononuclear U(IV) species in lacustrine sediment. *Geochim. Cosmochim. Acta* **222**,  
1102 171–186.
- 1103 Taylor R. M., Hansen H. C. B., Stanger G. and Koch C. B. (1991) On the genesis and  
1104 composition of natural pyroaurite. *Clay Minerals* **26**, 297–309.
- 1105 Thomassin J. H., and Touray J. C. (1982) L'hydrotalcite, un hydroxycarbonate transitoire  
1106 précocément formé lors de l'interaction verre basaltique-eau de mer. *Bull. Mineral.*  
1107 **105**, 312–319.
- 1108 Tosca N. J., Macdonald F. A., Strauss J. V., Johnston D. T. and Knoll A. H. (2011)  
1109 Sedimentary talc in Neoproterozoic carbonate successions. *Earth and Planetary*  
1110 *Science Letters* **306**, 11–22.
- 1111 Trittschack R., Grobety B. and Koch-Muller M. (2012) In situ high-temperature Raman and  
1112 FTIR spectroscopy of the phase transformation of lizardite. *American Mineralogist* **97**,  
1113 1965–1976.
- 1114 Turvey C. C., Wilson S. A., Hamilton J. L. and Southam G. (2017) Field-based accounting of  
1115 CO<sub>2</sub> sequestration in ultramafic mine wastes using portable X-ray diffraction.  
1116 *American Mineralogist* **102**, 1302–1310.
- 1117 Velde B. (2003) Green clay minerals. In *Treatise on geochemistry*, (eds. H. D. Holland and K.  
1118 K. Turekian), vol. 7. Elsevier, pp. 309–324
- 1119 Von Blanckenburg F., Mamberti M., Schoenberg R., Kamber B. S. and Webb G. E. (2008)  
1120 The iron isotope composition of microbial carbonate. *Chemical Geology* **249**, 113–  
1121 128.
- 1122 Wang J., Wang Z. Y., Ke W. (2013) A study of the evolution of rust on weathering steel  
1123 submitted to the Qinghai salt lake atmospheric corrosion. *Materials Chemistry and*  
1124 *Physics* **139**, 225–232.
- 1125 Webb G. E. and Kamber B. S. (2000) Rare earth elements in Holocene reefal microbialites: a  
1126 new shallow seawater proxy. *Geochim. Cosmochim. Acta* **64**, 1557–1565.
- 1127 Webb S. M. (2011) The MicroAnalysis Toolkit: X-ray Fluorescence Image Processing  
1128 Software. *AIP Conf. Proc.* **1365**, 196–199.
- 1129 Weber K. A., Achenbach L. A. and Coates J. D. (2006) Microorganisms pumping iron:  
1130 anaerobic microbial iron oxidation and reduction. *Nat. Rev. Micro.* **4**, 752–764.
- 1131 Wilkins R. and Ito J. (1967) Infrared Spectra of Some Synthetic Talcs. *Am. Miner.* **52**, 1649–  
1132 1660.
- 1133 Wilson S. A., Harrison A. L., Dipple G. M., Power I.M., Barker S.L.L., Mayer K.U., Fallon  
1134 S.J., Raudsepp M., Southam G. (2014) Offsetting of CO<sub>2</sub> emissions by air capture in  
1135 mine tailings at the Mount Keith Nickel Mine, Western Australia: Rates, controls and  
1136 prospects for carbon neutral mining. *International Journal of Greenhouse Gas Control*  
1137 **25**, 121–140
- 1138 Yariv S. and Heller-Kallai L. (1975) The Relationship between the I.R. Spectra of Serpentine  
1139 and Their Structures. *Clays and Clay Minerals* **23**, 145–152.
- 1140 Zeyen N., Benzerara K., Li J., Groleau A., Balan E., Robert J.-L., Estève I., Tavera R.,  
1141 Moreira D. and López-García P. (2015) Formation of low-T hydrated silicates in  
1142 modern microbialites from Mexico and implications for microbial fossilization.  
1143 *Frontiers in Earth Science* **3**.
- 1144 Zeyen N., Daval D., Lopez-Garcia P., Moreira D., Gaillardet J. and Benzerara K. (2017)  
1145 Geochemical Conditions Allowing the Formation of Modern Lacustrine Microbialites.  
1146 *Procedia Earth and Planetary Science* **17**, 380–383.
- 1147 Zimmer B. W., Riggs N. R. and Carrasco-Núñez G. (2010) Evolution of tuff ring-dome

1148 complex: the case study of Cerro Pinto, eastern Trans-Mexican Volcanic Belt. *Bulletin*  
1149 *of Volcanology* **72**, 1223–1240.  
1150

## FIGURE CAPTIONS

### **Figure 1.**

XANES spectra at the Fe K-edge of AL2014-15, AL66 and AL13 microbialites from Lake Alchichica. (a) Spectra of references (goethite, ferrihydrite, hydrotalcite, illite and nano-Fe(II):talc) are shown in colors. Spectra of the microbialites (black lines) are superimposed on fits (red lines) obtained by LC-LSF analysis. (b) Proportion of the fitting components: Fe(III):hydrotalcite as a proxy for pyroaurite/iowaite, goethite and ferrihydrite as proxies for Fe (oxyhydr)oxides, nano-Fe(II): and nano-Fe(III):talc as proxies for nanocrystalline 2:1 trioctahedral phyllosilicates, Fe(III)-bearing illite as proxy for 2:1 dioctahedral phyllosilicates.

### **Figure 2.**

Powder X-ray diffraction patterns of Alchichica microbialite samples. (a) AL2014-15, AL66 and AL13 microbialite samples. Aragonite (A), hydromagnesite (H) and layered double hydroxide (LDH) were detected. (b-c) Close-ups on the LDH peaks at 7.59 Å (13.4° 2 $\theta$ ) and 3.79 Å (27.3° 2 $\theta$ ) observed in the pattern of AL2014-15, outlined by red rectangles.

### **Figure 3.**

FTIR analyses of Alchichica microbialites. (a) FTIR spectra of AL2014-15, AL66 and AL13 between 400 and 1800 cm<sup>-1</sup>. Labels are as follows: aragonite (A), hydromagnesite (H) and layered double hydroxide (LDH). (b) FTIR spectra from 3000 to 4000 cm<sup>-1</sup>. (c) Close-up of the band at 1384.5 cm<sup>-1</sup> for AL66 and AL13, interpreted as a carbonate asymmetric stretching mode ( $\nu_3\text{CO}_3$ ) in LDH or aragonite.

### **Figure 4.**

1176 XANES spectra at the Fe K-edge of microbialites from La Preciosa, Atexcac, La Alberca de  
1177 Los Espinos and Pátzcuaro. **(a)**. Spectra of the microbialites (black lines) are superimposed on  
1178 fits (red lines) obtained by LC-LSF analysis **(b)** Proportion of the fitting components: nano-  
1179 Fe(II):talc and nano-Fe(III):talc as proxies for nanocrystalline 2:1 trioctahedral phyllosilicate,  
1180 and Fe(III):illite as proxy for 2:1 dioctahedral phyllosilicate.

1181

1182 **Figure 5.**

1183 Powder X-ray diffraction patterns of microbialites from Lakes La Preciosa, Atexcac, La  
1184 Alberca de Los Espinos and Pátzcuaro. Aragonite (A), calcite (C), monohydrocalcite (MC),  
1185 hydromagnesite (H) and kerolite/stevensite (K/S) were detected.

1186

1187 **Figure 6.**

1188 FTIR spectra of microbialites from Lakes La Preciosa, Atexcac, La Alberca de Los Espinos  
1189 and Pátzcuaro. **(a)** Spectra from 400 to 1800  $\text{cm}^{-1}$  **(b)** Spectra from 3000 to 4000  $\text{cm}^{-1}$ . **(c)**  
1190 Close-up of the spectral area between 1372 and 1395  $\text{cm}^{-1}$ . The peak at 1384.5  $\text{cm}^{-1}$  indicated  
1191 by a dashed line was assigned to carbonate asymmetric stretching in LDH and/or aragonite.  
1192 Peak labels are as follows: aragonite (A); calcite (C); monohydrocalcite (MC);  
1193 hydromagnesite (H); layered double hydroxide (LDH) and kerolite/stevensite (K/S).

1194

1195 **Figure 7.**

1196 Light microscopy observations of Fe spatial distribution in the microbialites. **(a-b)** Plane- and  
1197 cross-polarized light photomicrographs of AL2014-15 sample showing dense masses and Fe-  
1198 rich fine discrete laminae (arrows). **(c-d)** Plane- and cross-polarized light photomicrographs  
1199 of AL13 showing layers of a brownish Fe-bearing phase between aragonite (A) and  
1200 hydromagnesite (H) as well within hydromagnesite (white dashed arrow). **(e-f)** Plane- and



cross-polarized light photomicrographs of ATX-2C1-2012 showing a beige Fe-bearing phase forming a ~20 to 100  $\mu\text{m}$  thick layer at the surface of the microbialite. This phase shows total extinction under cross-polarized light. **(g-h)** Plane- and cross-polarized light photomicrographs of Patz2014-02 showing brown Fe-bearing laminae measuring ~50 to 150  $\mu\text{m}$  in thickness (white arrow) and showing extinction under cross polars. A darker Fe-rich area is also observed (white dashed arrow).

**Figure 8.**

Analysis of Fe distribution in AL66 by correlative electron/x-ray microscopy. **(a)** SEM image acquired in the BSE (backscattered electron) mode. Labels are as follows: aragonite (A) and hydromagnesite (H). **(b)**  $\mu$ -XRF mapping of Fe (red) and Ca (green) in AL66 in the area outlined by a dashed rectangle in (a). **(c)** SEM image in backscattered electron mode of the area outlined by a rectangle in (b). Resin appears on the left. Aragonite (A) and hydromagnesite (H) are separated by a Fe-rich phase showing a darker contrast compared to aragonite due to the presence of lighter element(s). The red rectangle indicates the localization of the FIB section cutting across a Fe-rich lamina. **(d)** Overlay of the Fe (red), Mg (blue) and Ca (green) SEM-EDXS maps. The Fe-rich phase appears in pink (i.e. a combination of Fe and Mg).

**Figure 9.**

Transmission electron microscopy analyses of a FIB foil cut across aragonite and the Fe-rich phase in AL66, outlined in Fig. 8c. **(a)** STEM-HAADF image of the FIB foil. **(b)** STEM-EDXS map of Fe (red), Mg (blue) and Ca (green) of the same area. The Fe-rich phase appears in pink (i.e. a combination of Fe and Mg). **(c)** Selected area electron diffraction (SAED) pattern of the circled area #1 on Fig. 9b. Diffuse diffraction spots and arcs were indexed as

lattice planes of LDH and aragonite (A), as indicated on the pattern. **(d)** SAED pattern of aragonite (area #2 as indicated on Fig. 9b). Radial intensity profile is shown in Fig. SI-7. **(e)** EDXS spectra of the circled areas noted (1) and (2) on Fig. 9b, corresponding to the Fe-rich area (composed by Fe, Mg and Cl) and aragonite, respectively (Cu peaks were emitted by the Cu grid to which the FIB foil was attached).

#### **Figure 10.**

Analysis of Fe distribution in AL13 by correlative electron/x-ray microscopy. **(a)** SEM backscattered electron image. **(b)**  $\mu$ -XRF mapping of the area outlined by a rectangle in Fig. 10a. Fe and Ca are shown in red and green, respectively. **(c)** SEM backscattered electron image of the area outlined by a rectangle in Fig. 10b. The red rectangle indicates the localization of the FIB section cutting across a Fe-rich lamina. **(d)** SEM-EDXS map of the same area showing Fe, Mg and Ca in red, blue and green, respectively.

#### **Figure 11.**

Transmission electron microscopy analyses of a FIB foil extracted from AL13 (see rectangle in Fig. 10c). **(a-b)** STEM-HAADF images of the FIB foil. **(c)** STEM-EDXS mapping of the area outlined by a dashed rectangle in Fig. 11a and showing two distinct mineral phases. Iron, Ca and Mg are shown in red, green and blue, respectively. **(d)** EDXS spectrum of the area outlined by a white circle in Fig. 11c. **(e)** SAED pattern of the same area circled in Fig. 11c. **(f)** STXM Fe map of the FIB foil obtained by subtracting an image at 704 eV (below the Fe  $L_{2,3}$ -edges) from an image at 709.7 eV (above the Fe  $L_3$ -edge). **(g)** XANES spectrum at the Fe  $L_{2,3}$ -edges extracted from the area outlined in Fig. 11f. **(h)** STXM map of two C-bearing species observed in the area outlined by a dashed rectangle in Fig. 11a, and discriminated based on their XANES spectra at the C K-edge. Aragonite appears in green, while LDH

appears in red. (i) XANES spectrum at the C K-edge of the LDH, observed in red in Fig. 11h.

## **Figure 12.**

SEM analysis of the Fe distribution in AL2014-15. (a) SEM backscattered electron image. The red rectangle indicates the localization of the FIB section cutting across two circular objects. (b) SEM-EDXS map of the area outlined by a dashed rectangle in Fig. 12a. Fe, Ca and Mg are shown in red, green and blue, respectively. Aragonite (A) and hydromagnesite (H) are surrounding by large Fe- and Si-rich areas. (c) SEM-EDXS map of Si corresponding to the area outlined in Fig. 12a.

## **Figure 13.**

TEM analyses of a FIB foil extracted from AL2014-15 as outlined in Fig. 12a. (a) Bright-field TEM image showing an object with a circular cross-section. (b) STEM-HAADF image of the object showed in Fig. 13a. (c) EDXS spectra of areas #1 and # 2, outlined in Fig. 13b. (d) SAED pattern of area outlined in Fig. 13a corresponding to area #1: LDH viewed along the [1-1-1] zone axis. The  $d$ -spacings at 2.66 Å, 1.55 Å and 1.30 Å corresponded to LDH (-10-1), (-1-10) and (-20-2) lattice planes. (e) SAED pattern of area outlined in Fig. 13a corresponding to area #2: silico-ferric precipitate as synthesized by Decarreau et al. (1987) and/or ferrihydrite.  $D$ -spacings at 3.15, 2.36 and 1.49 Å are identified. (f) Bright-field TEM image of the second object with a circular cross-section. (g) Close-up of the fibrous layer surrounding the object structures as outlined by a dashed rectangle in Fig. 13f. (h) SAED pattern of area 3 circled in Fig. 13f: aragonite with  $d$ -spacings at 2.48, 1.87, 1.25, 1.12 Å.

## **Figure 14.**

SEM observations of Fe-bearing silicates in ATX-2C1-2012, AlbEsp2014-01 and Patz2014-

02. (a-b-c) SEM backscattered electron images. (d-e-f) EDXS spectra of the areas outlined by a circle in SEM images. Platinum (Pt) was used to sputter-coat AlbEsp2014-01.

**Figure 15.**

SEM and TEM analyses of ATX-2C1-2012. (a) SEM backscattered electron image. (b) SEM-EDXS map of the area outlined in (a). Fe and Ca are shown in red and green, respectively. (c) STEM-HAADF image of the FIB foil extracted from the area outlined by a red rectangle in (a). (d) Bright-field TEM image showing the smooth texture of the Fe-rich phase and the micritic texture of aragonite. (e) SAED pattern of the Fe-rich phase, as outlined by a circle in (d). (f) STEM-HAADF close-up of the area outlined in (d). (g) STEM-EDXS map of the same area. Fe, Ca and Mg are shown in red, green and blue. (h) EDXS spectrum of the area circled in (d) and corresponding to the Fe-rich phase.

**Figure 16.**

STXM analyses of a FIB foil extracted from ATX-2C1-2012. (a) STXM Fe map obtained by subtracting an image at 700 eV converted in optical density (below the Fe L<sub>2,3</sub>-edges) from an OD-converted image taken at 710 eV. (b) XANES spectrum at the Fe L<sub>2,3</sub>-edges of the Fe-rich area outlined by a white circle in (a). (c) XANES spectrum at the C K-edge of the Fe-rich area outlined by an orange circle in (a).

**Figure 17.**

Schematic diagram suggesting the origin of pyroaurite precipitation in Lake Alchichica. (1) Basalt alteration by groundwater, releasing Fe(II) (2) Fast oxidation of Fe(II) at the contact with lake water, rich in Cl<sup>-</sup>, Mg<sup>2+</sup>, and CO<sub>3</sub><sup>2-</sup> and showing a high pH resulting in pyroaurite/iowaite precipitation (3).

**Table 1.**  
Summary of the main physical and geochemical parameters of the lakes

Lakes	Predominant ions	Conductivity (mS/cm)	pH	Alk (mM)	Mg (mM)	Cl (mM)	H <sub>4</sub> SiO <sub>4</sub> (mM)	Ca (mM)	References
Alchichica (North shore)	Cl(+HCO <sub>3</sub> )-Na	13.3	8.8	30.9	17.8	87.3	0.015	0.368	Kázmierczak et al., 2011
Alchichica (West shore)	Bic(+Cl)-Na	2.1	7.3	9.34	3.7	5.47	0.694	1.670	Kázmierczak et al., 2011
La Preciosa (surface)	Bic-Mg	2.2	8.6	14.4	8.23	9.31	0.50	0.349	Armienta et al., 2008
Atexcac (surface)	Cl(+HCO <sub>3</sub> )-Na	11.7	8.2	28.3	23.1	96.6	0.95	1.070	Kázmierczak et al., 2011
Alberca de Los Espinos (surface)	Bic(+Cl)-Na	1.25	8.7	7.64	2.55	4.77	0.87	0.920	Our data; Zeyen et al., 2017
Pátzcuaro (surface)	Na-Bic	0.98	8.2	11.04	1.48	3.0	0.45	0.549	Sigala et al., 2017

**Table 2.**  
Bulk chemical composition of studied microbialites (in wt.%)

Sample	Fe	Al	K	Ti	Na	P	Mn	Mg	Si	Ca
AL2014-15	2.24 ± 0.04	0.12 ± 0.02	0.07 ± 0.01	< 0.01	0.46 ± 0.02	0.040 ± 0.004	0.010 ± 0.001	6.3 ± 0.1	1.02 ± 0.05	23.6 ± 0.5
AL13	0.12 ± 0.01	0.22 ± 0.02	0.06 ± 0.01	< 0.01	0.20 ± 0.03	< 0.02	< 0.0002	22.2 ± 0.4	0.65 ± 0.03	4.0 ± 0.1
Preciosa05-2012	0.31 ± 0.02	0.63 ± 0.06	0.16 ± 0.02	0.03 ± 0.01	0.29 ± 0.04	< 0.02	0.040 ± 0.004	7.0 ± 0.1	11.3 ± 0.1	19.0 ± 0.4
ATX-2C1-2012	0.54 ± 0.03	0.29 ± 0.03	0.11 ± 0.01	0.02 ± 0.01	0.33 ± 0.05	< 0.02	0.040 ± 0.004	12.8 ± 0.3	13.9 ± 0.1	9.1 ± 0.2
AlbEsp2014-01	0.38 ± 0.02	0.06 ± 0.01	0.02 ± 0.01	< 0.01	0.04 ± 0.01	0.27 ± 0.03	0.46 ± 0.02	3.5 ± 0.1	3.3 ± 0.2	28.7 ± 0.6
Patz2014-02	0.62 ± 0.03	0.35 ± 0.04	0.04 ± 0.01	0.02 ± 0.01	0.09 ± 0.01	0.07 ± 0.01	0.120 ± 0.006	5.5 ± 0.1	6.99 ± 0.07	25.2 ± 0.5

Table 3.

Result of the best fits of the Fe K-edge XANES spectra of the microbialite samples, expressed as the relative proportion of the model compounds components. The quality of the LCF fits was estimated by a reduced chi-square parameter  $\chi^2_R = n / (n-p) \sum [\mu_{exp} - \mu_{calc}]^2$  where p is the number of fitting components and n is the number of independent parameters corresponding to the energy range divided by the natural width of the U LIII or Fe K levels reported by Krause and Oliver (1979). Figures between brackets indicate 2σ confidence intervals (2\*standard deviation).

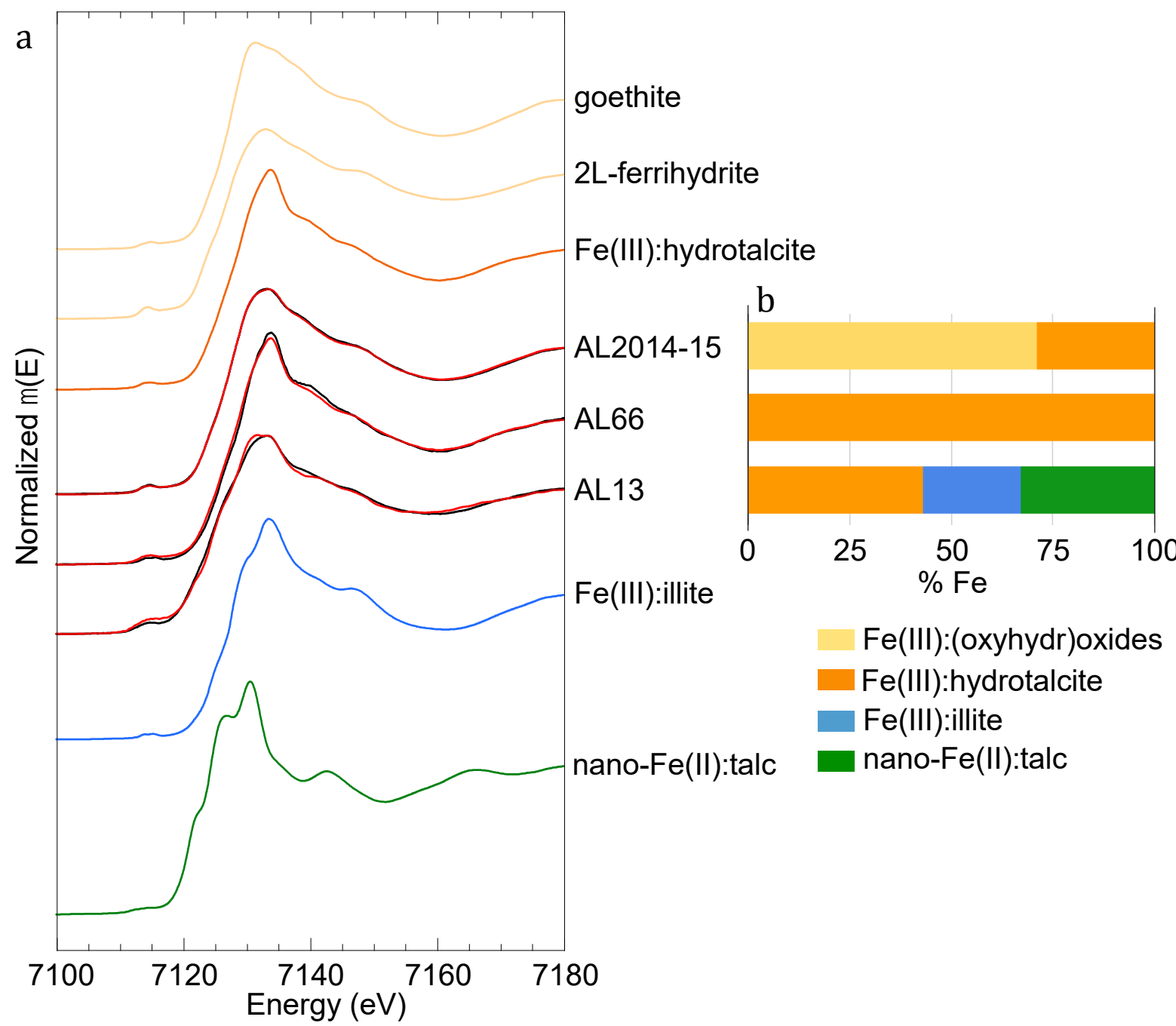
Sample	goethite	2L-ferrihydrite	Fe(III):hydrotalcite	nano-Fe(II):talc	nano-Fe(III):talc	Fe(III):illite	$\chi^2_R$	Fe(III)/Fe <sub>tot</sub>
AL2014-15	47 (4)	24 (5)	29 (3)	–	–	–	0.0003	1.0
AL66	–	–	100 (1)	–	–	–	0.0047	1.0
AL13	–	–	43 (19)	33 (3)	–	24 (19)	0.0040	0.7
Preciosa05-2012	–	–	–	26 (3)	43(16)	31 (15)	0.0045	0.7
ATX-2C1-2012	–	–	–	22 (2)	51 (11)	27 (10)	0.0021	0.8
AlbEsp2014-01	–	–	–	9 (1)	48 (9)	43 (9)	0.0015	0.9
Patz2014-02	–	–	–	10(1)	47 (4)	43 (4)	0.0003	0.9

**Table 4.**  
Summary of the mineralogical composition of the microbialite samples analyzed in this study.  
The identity of the Fe-bearing mineral phases is indicated.

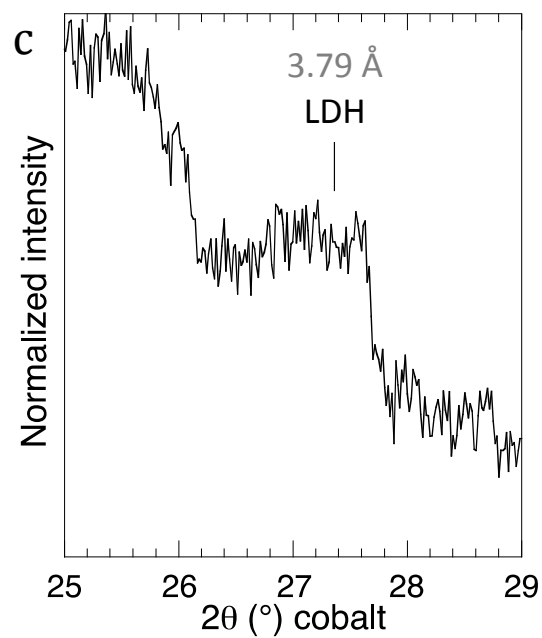
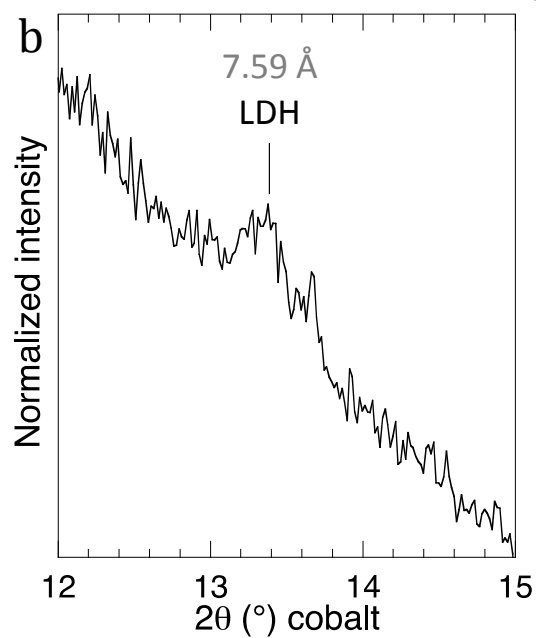
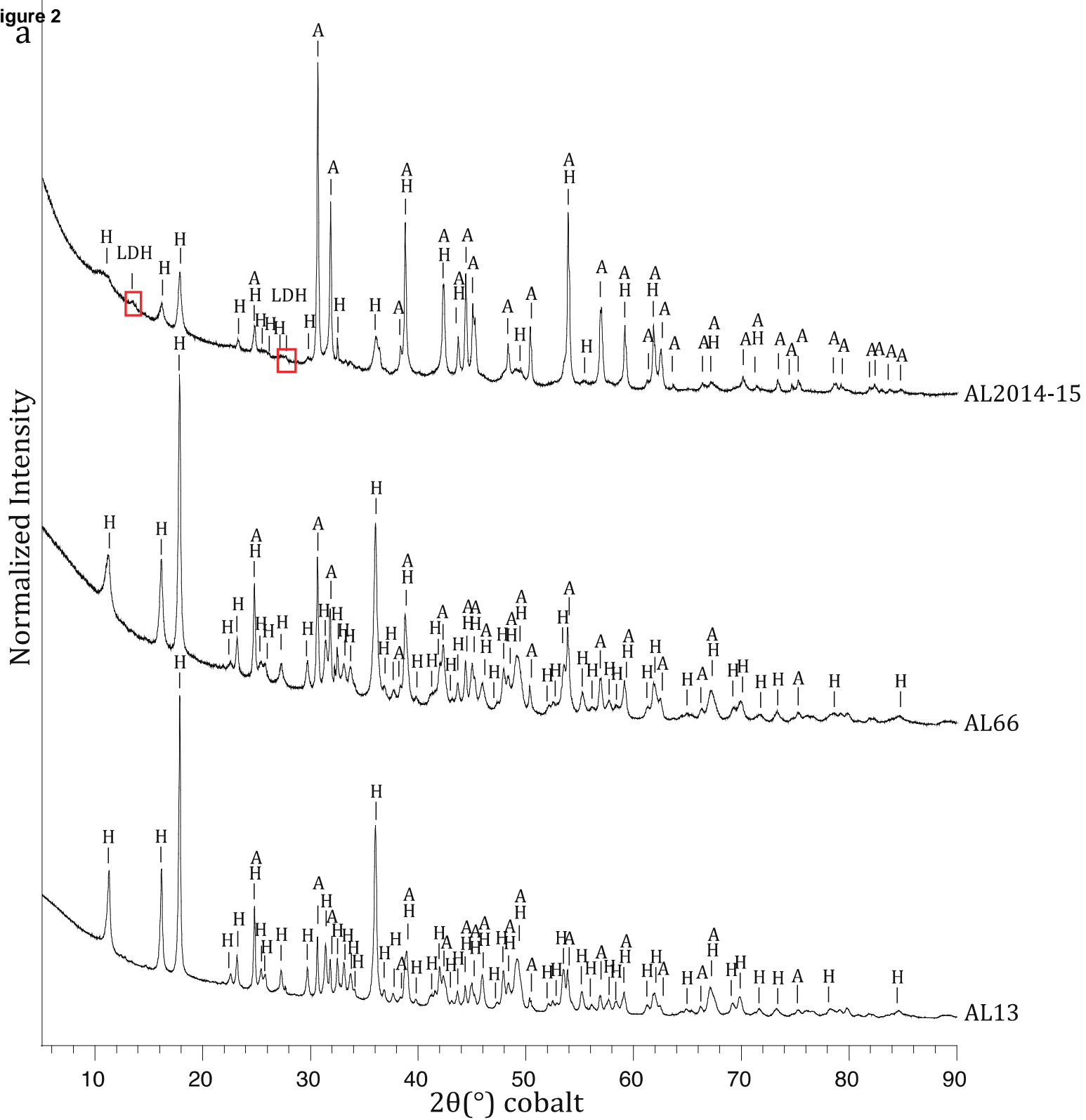
Sample	Main minerals (DRX-FTIR)	Authigenic Fe-bearing phase (XANES, DRX, FTIR, MEB, MET, SAED)
AL2014-15	aragonite– hydromagnesite – LDH	pyroaurite/iowaite – ferrihydrite – goethite
AL66	hydromagnesite – aragonite	pyroaurite/iowaite
AL13	hydromagnesite – aragonite	pyroaurite/iowaite – dioctahedral 2:1 phyllosilicate
Preciosa05-2012	aragonite – kerolite/stevensite – calcite	kerolite/stevensite – dioctahedral 2:1 phyllosilicate
ATX-2C1-2012	kerolite/stevensite – aragonite – calcite – hydromagnesite	kerolite/stevensite – dioctahedral 2:1 phyllosilicate
AlbEsp2014-01	calcite – monohydrocalcite – kerolite/stevensite	kerolite/stevensite – dioctahedral 2:1 phyllosilicate
Patz2014-02	calcite – aragonite – monohydrocalcite – kerolite/stevensite	kerolite/stevensite – dioctahedral 2:1 phyllosilicate



Figure 1



Normalized Intensity



**Figure 3**

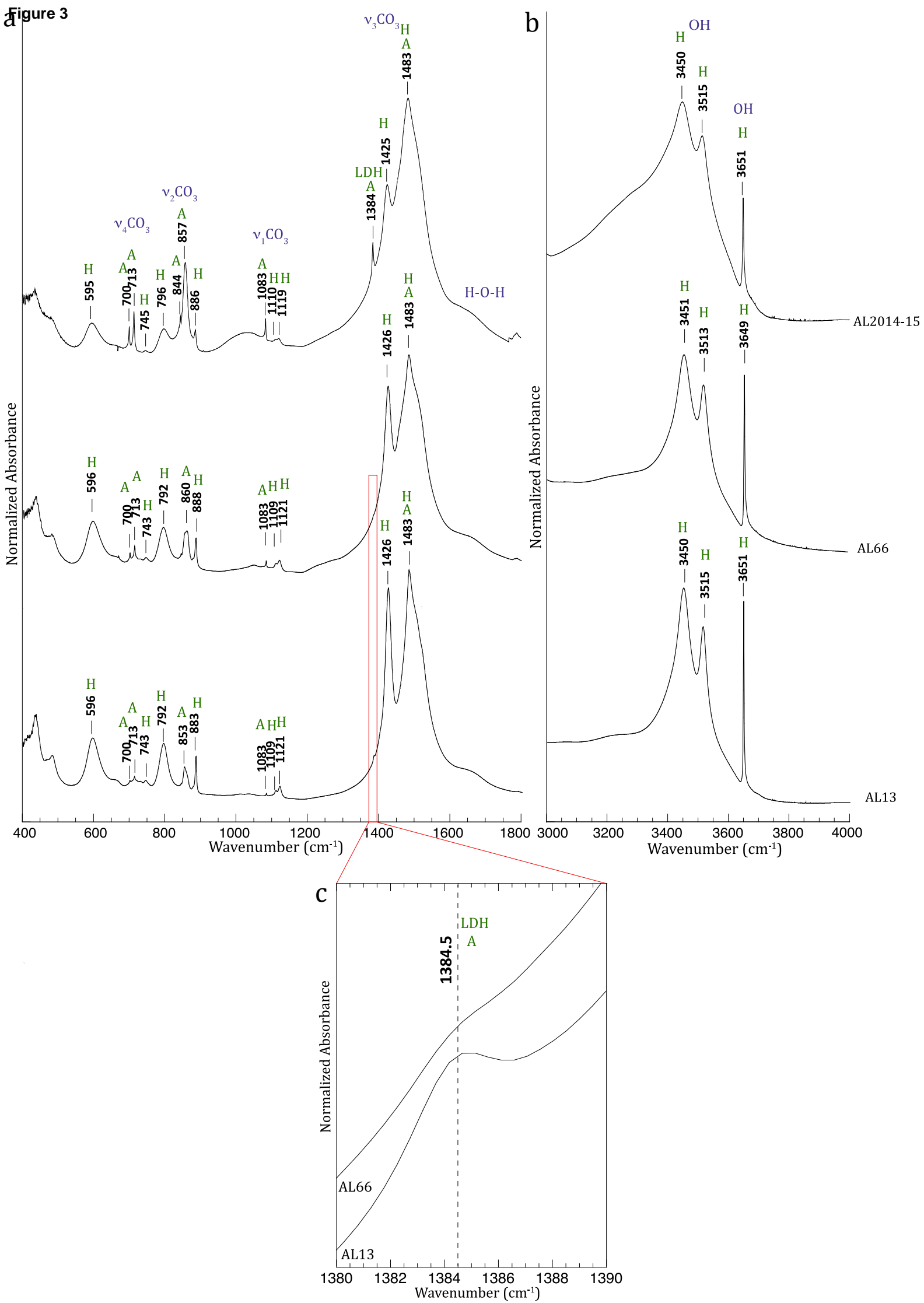


Figure 4

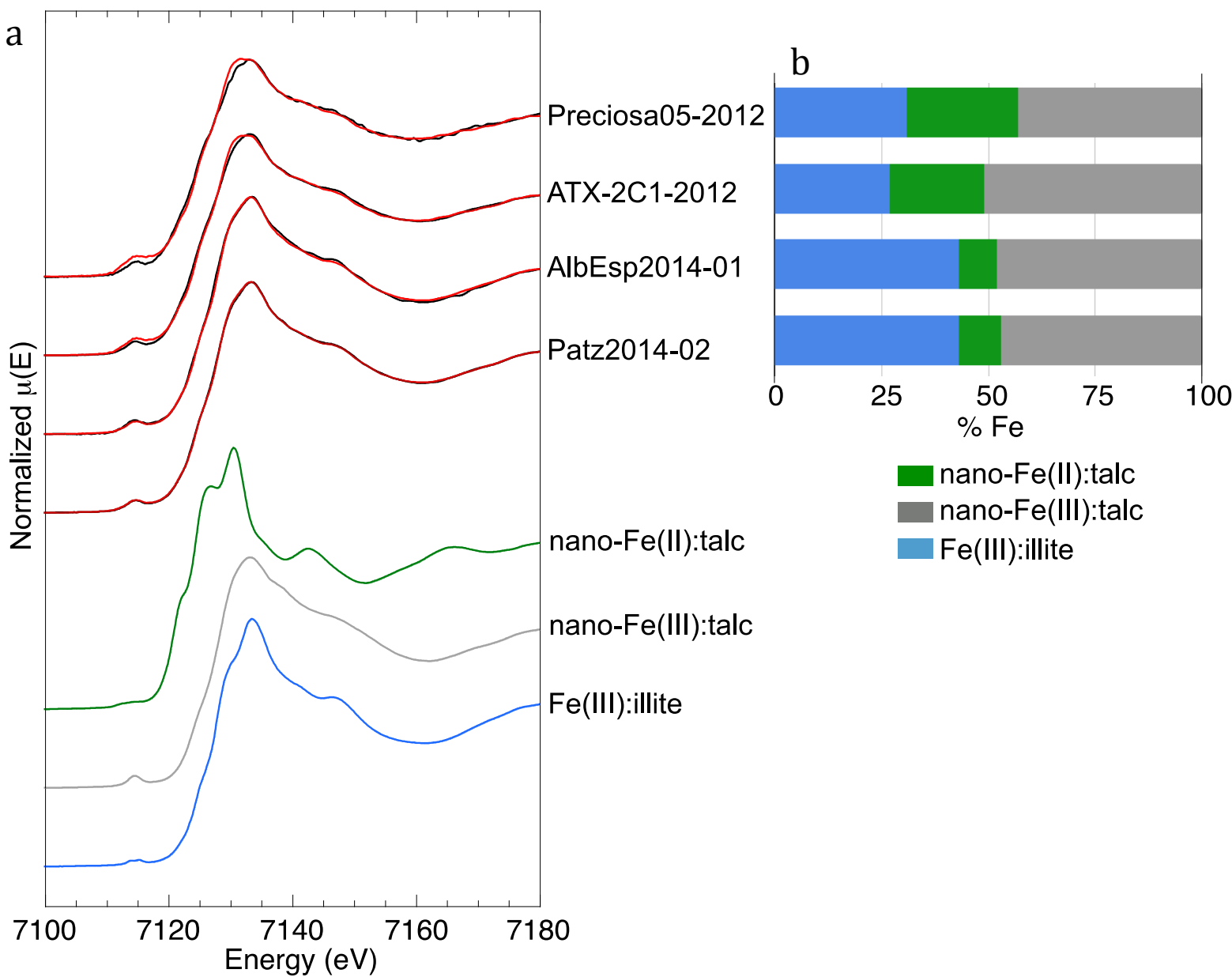


Figure 5

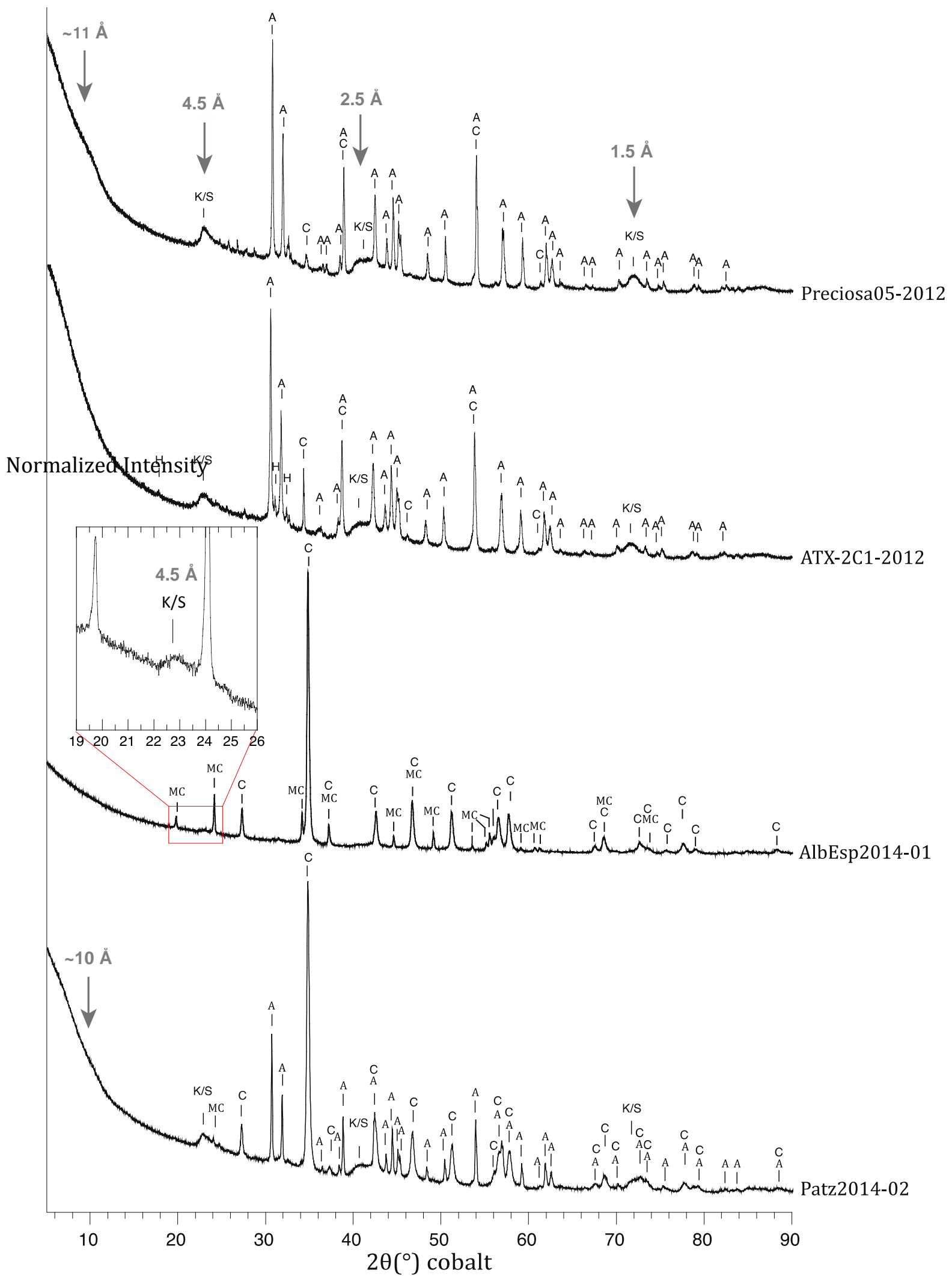
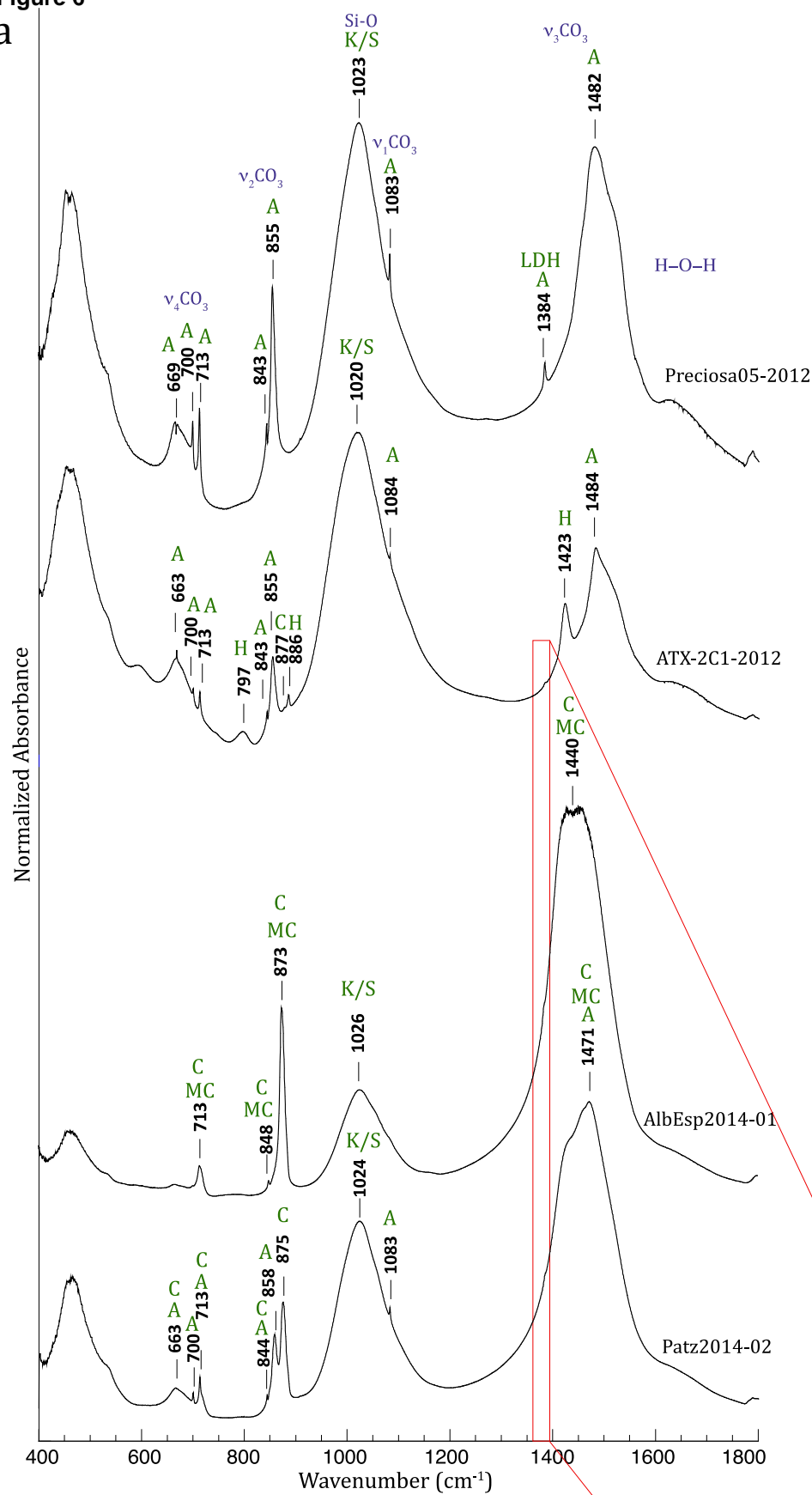
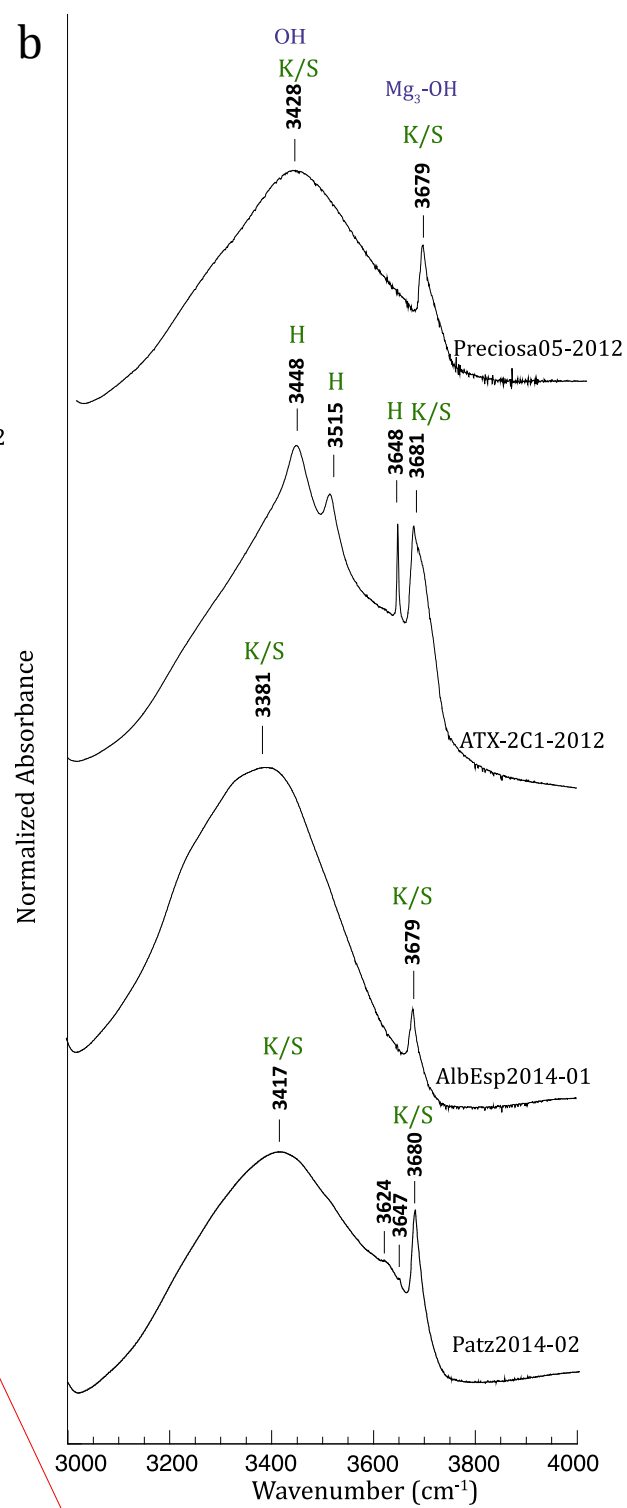


Figure 6

a



b



c

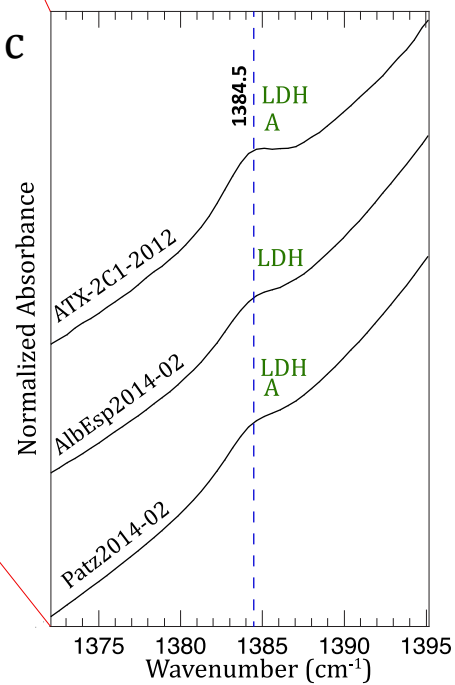




Figure 7

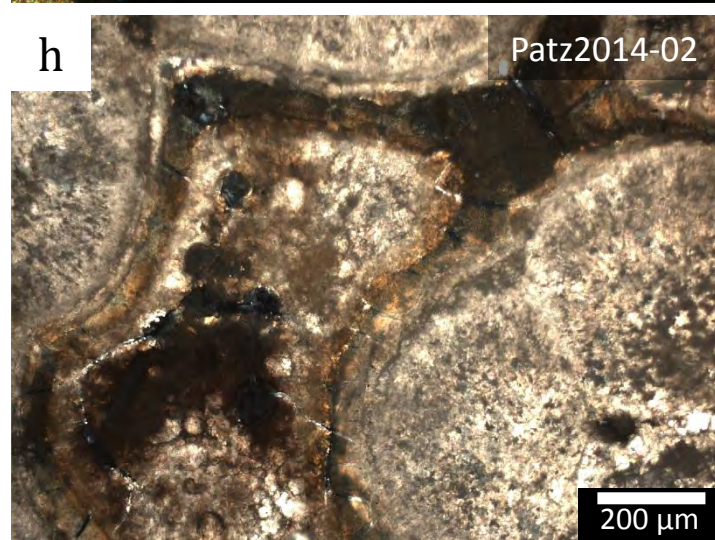
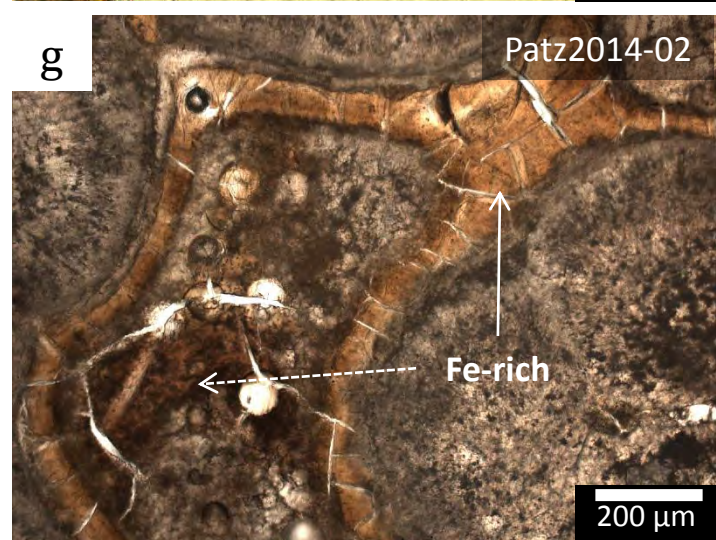
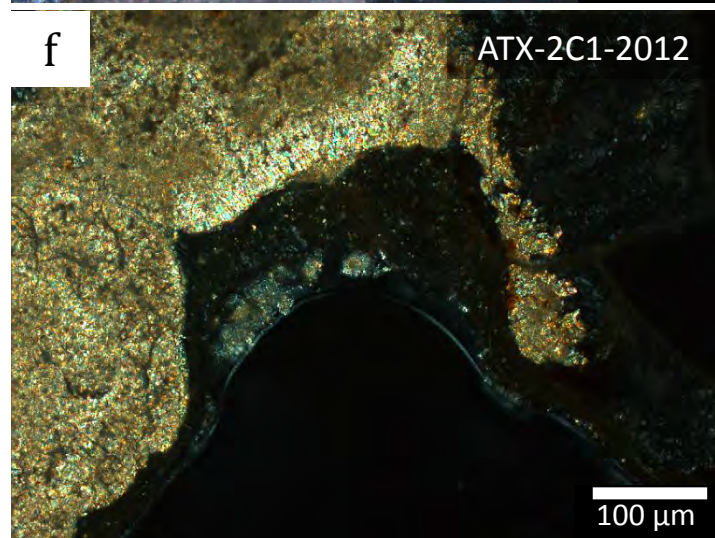
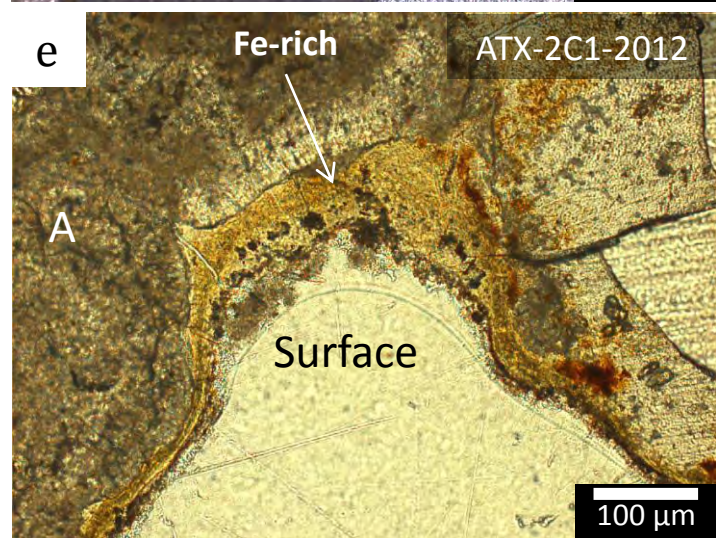
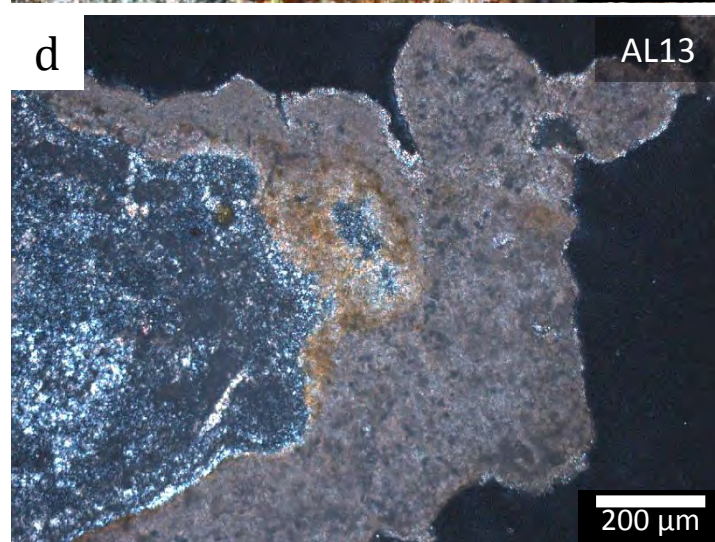
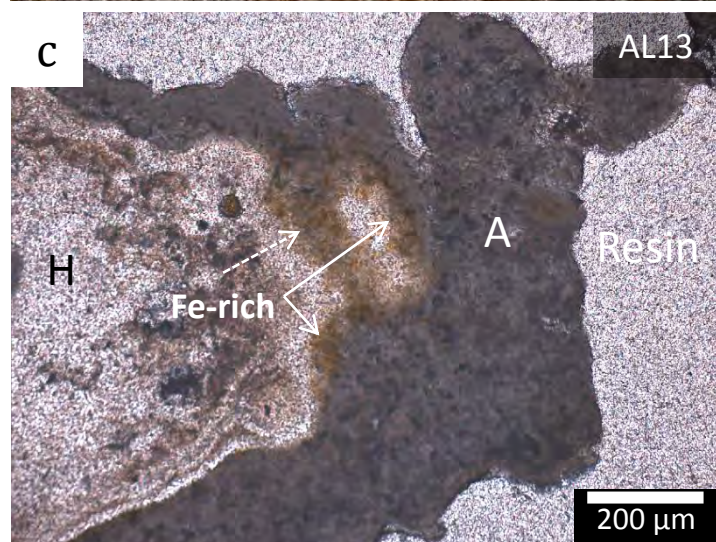
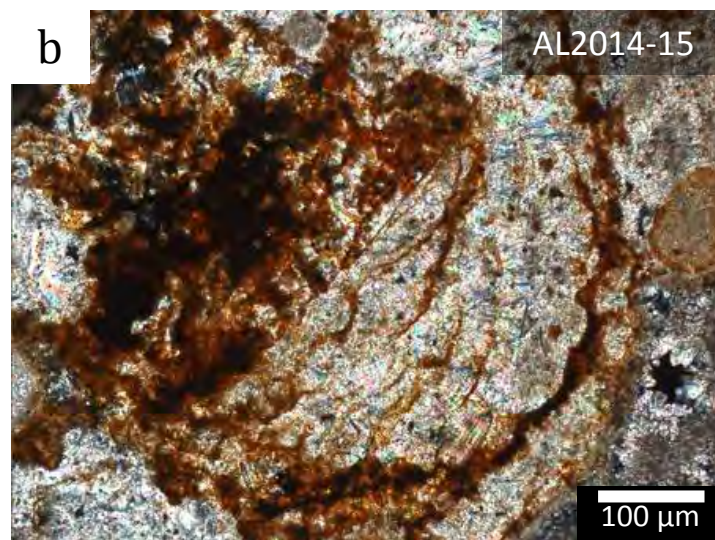
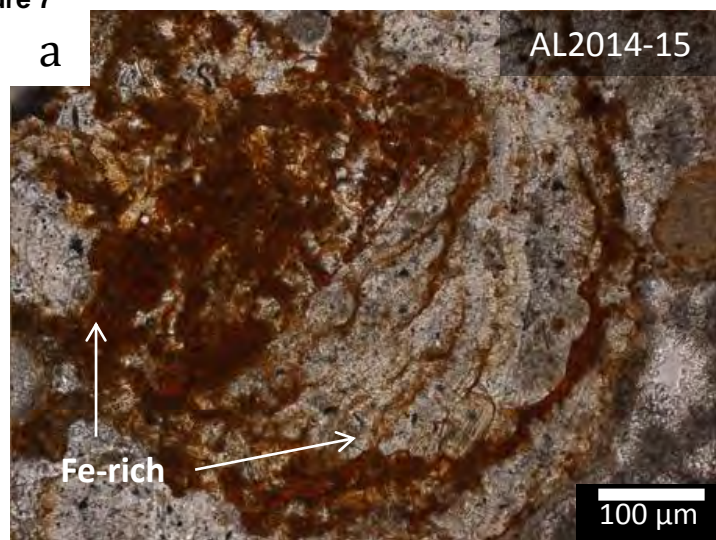




Figure 8

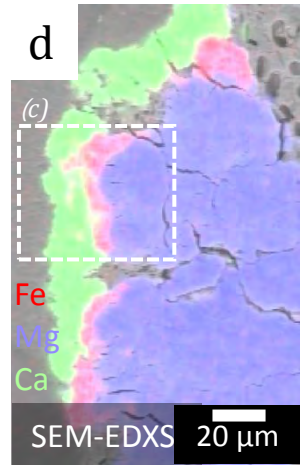
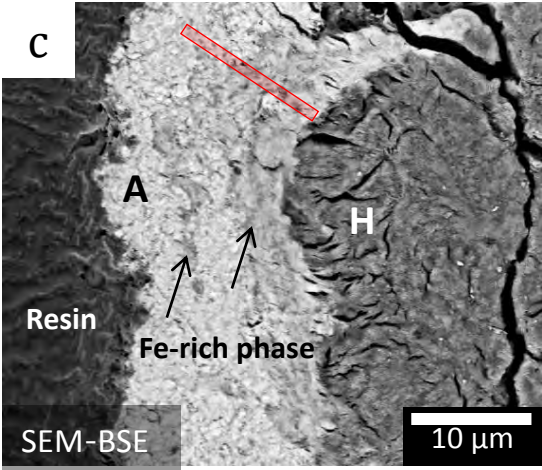
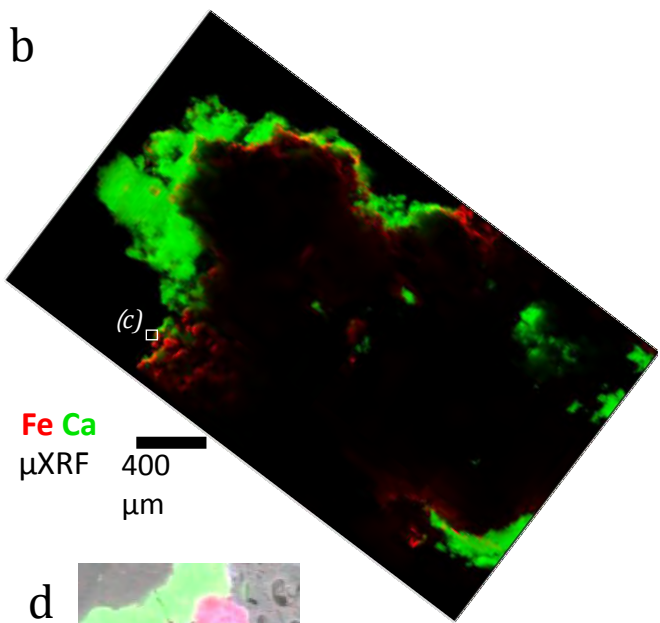
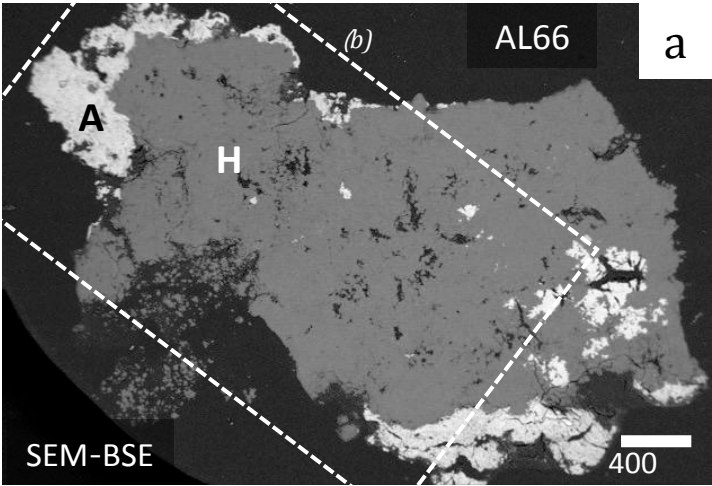




Figure 9

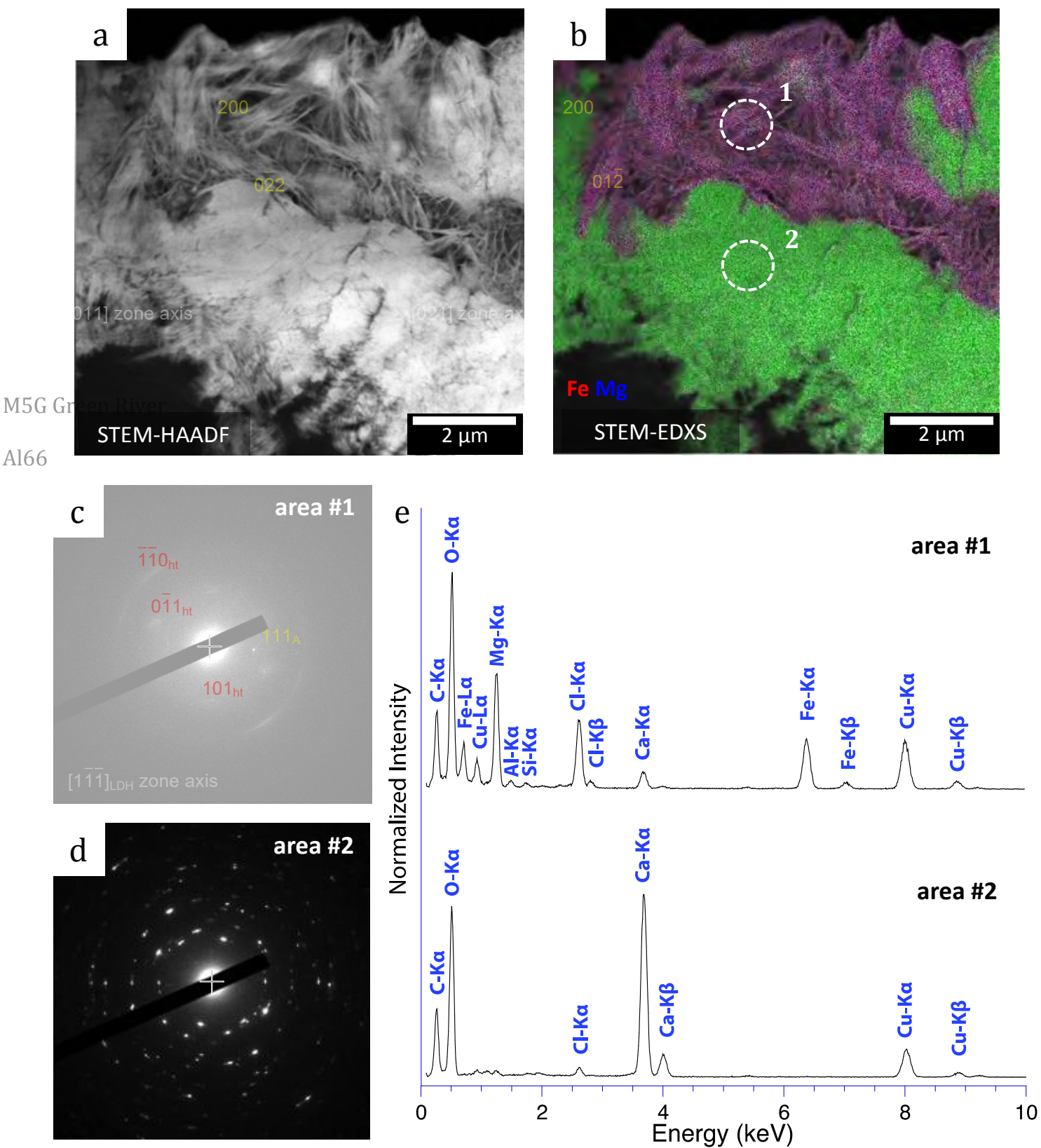


Figure 10

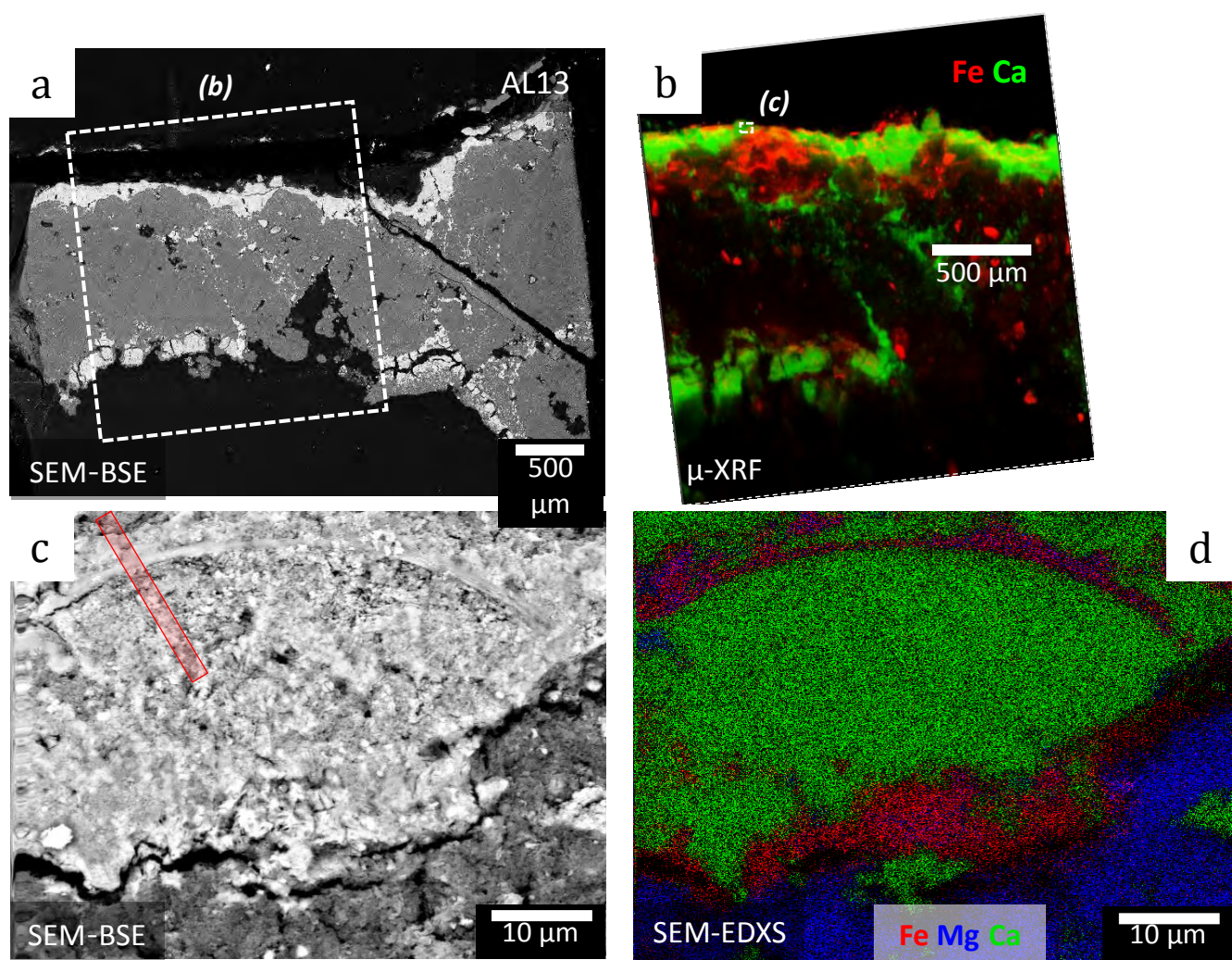


Figure 11

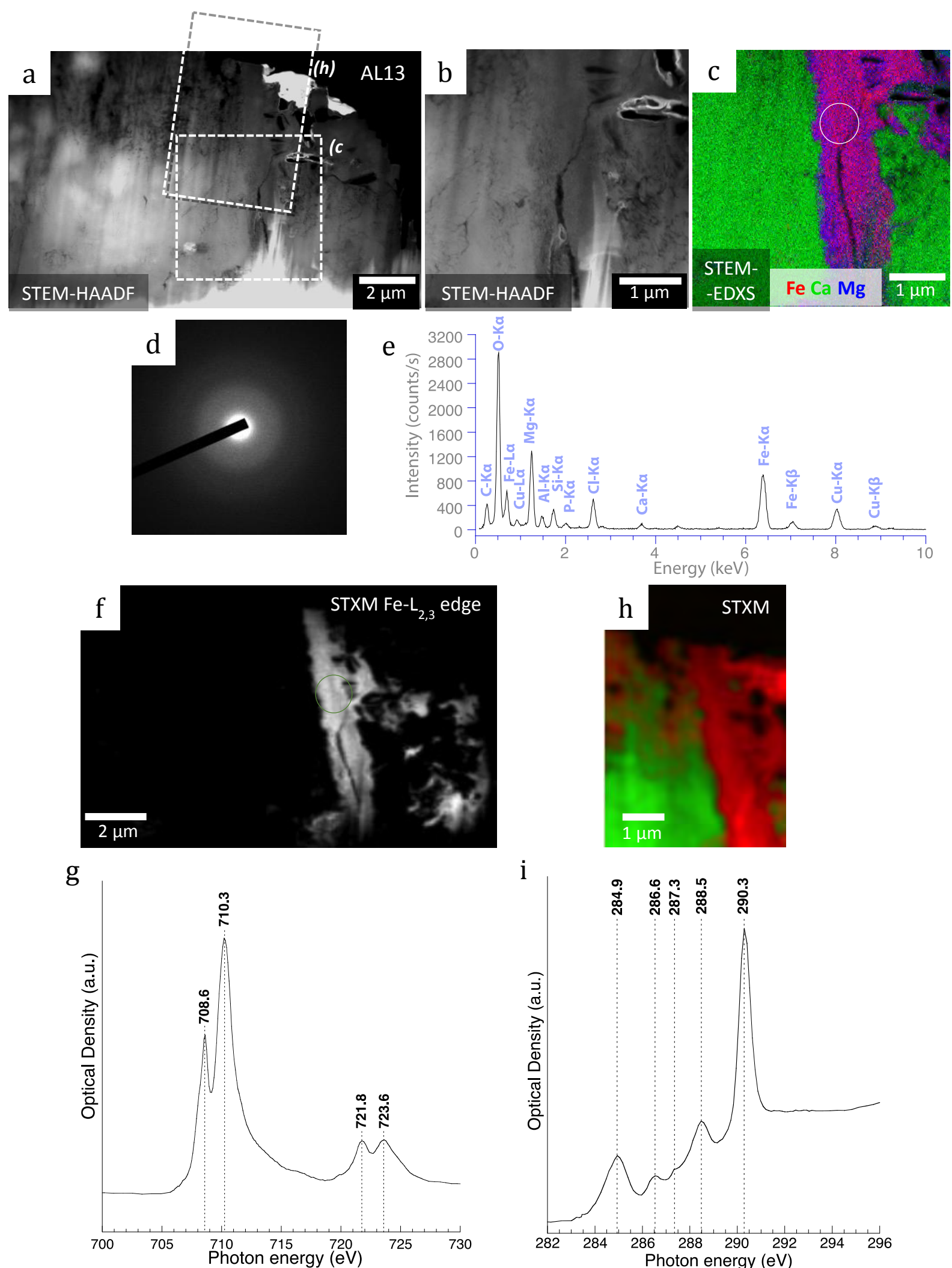




Figure 12

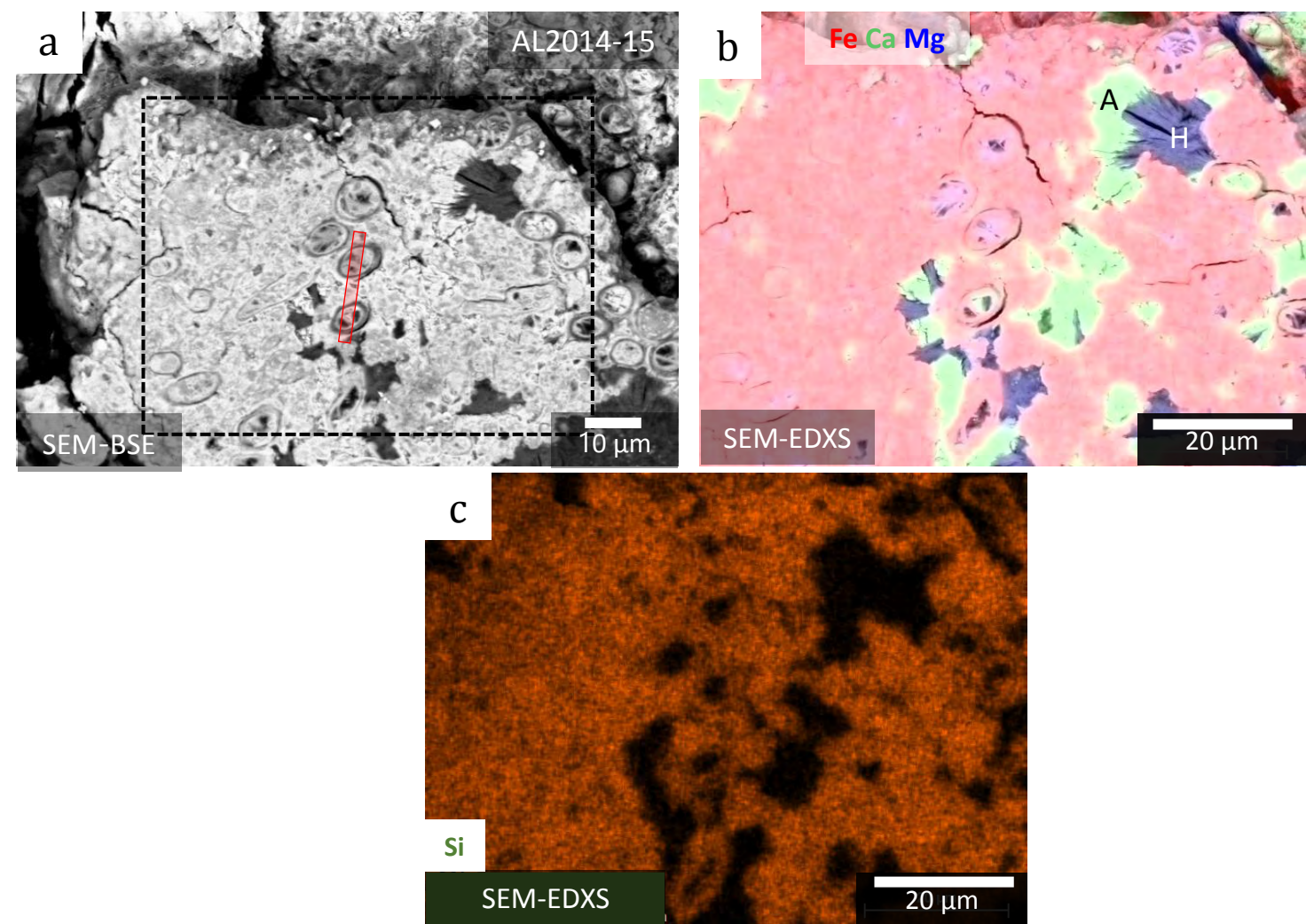


Figure 13

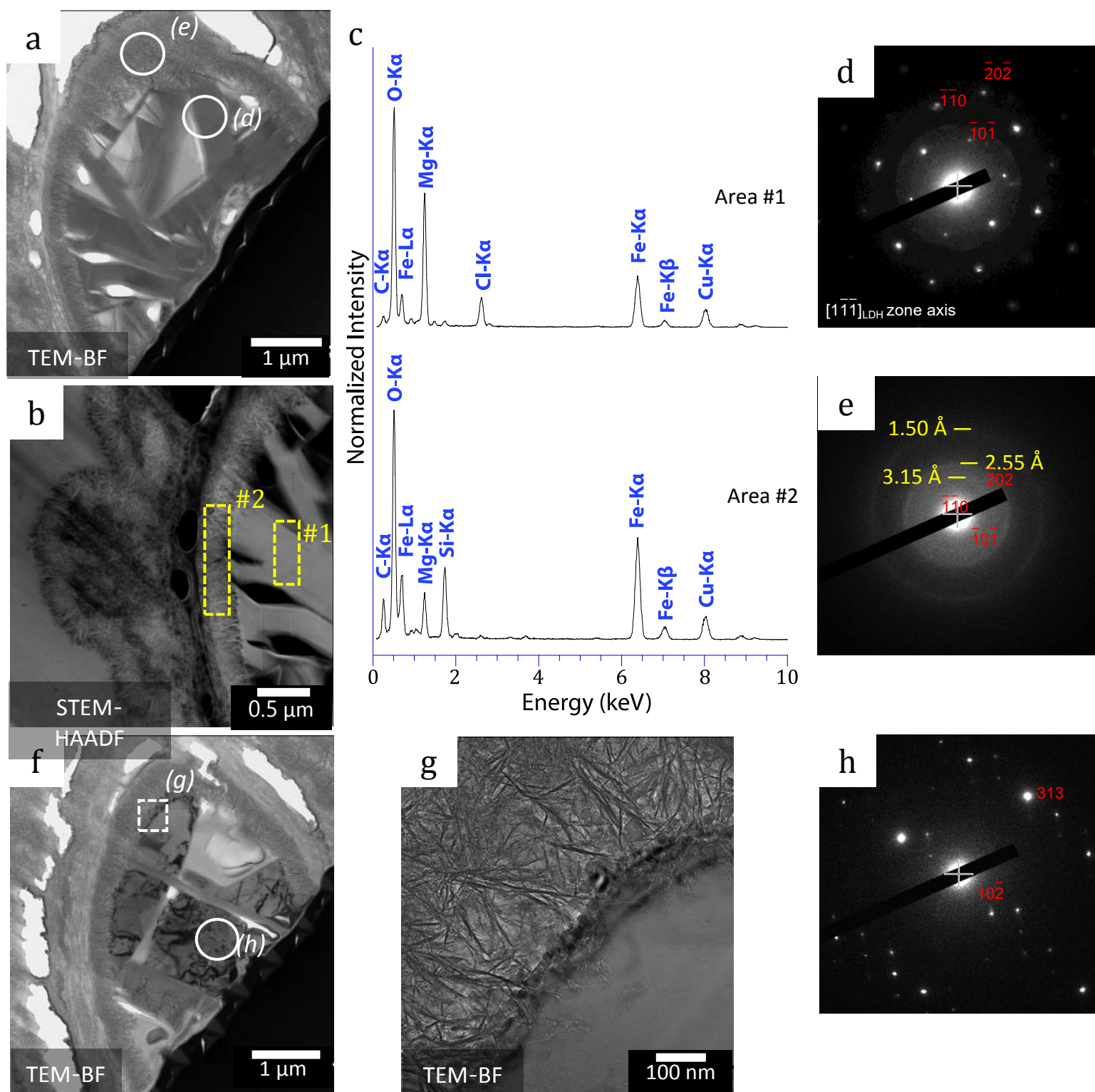


Figure 14

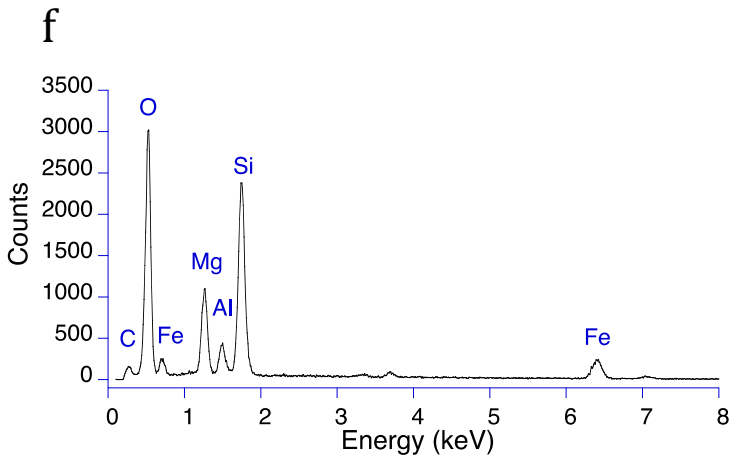
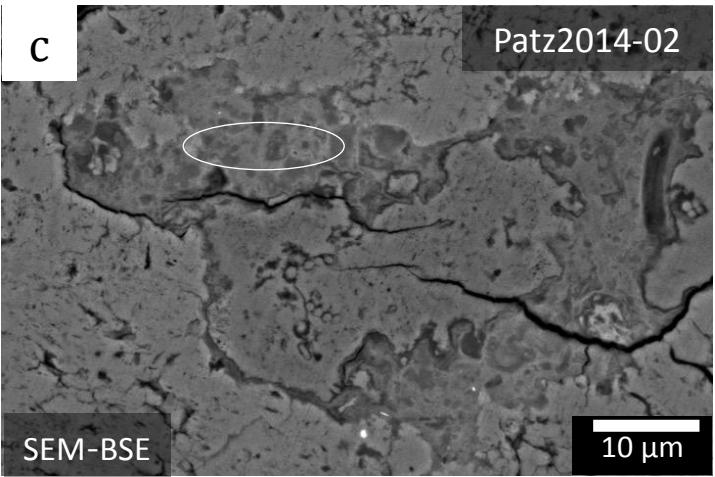
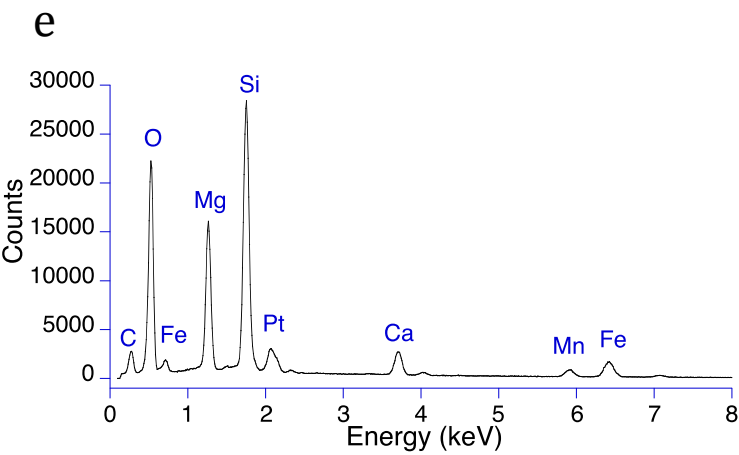
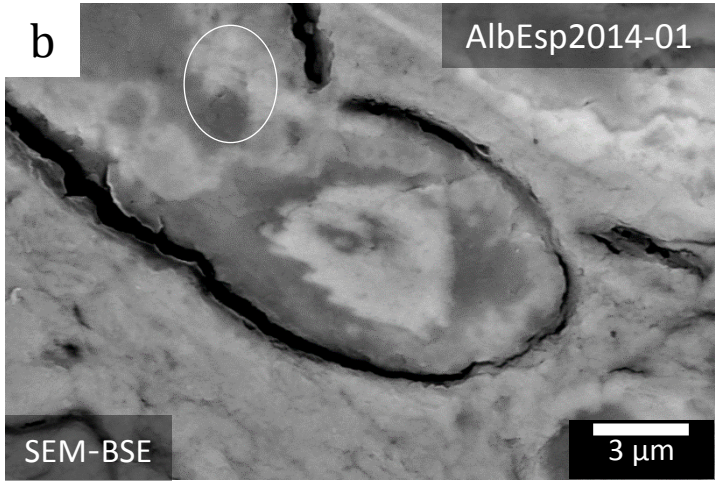
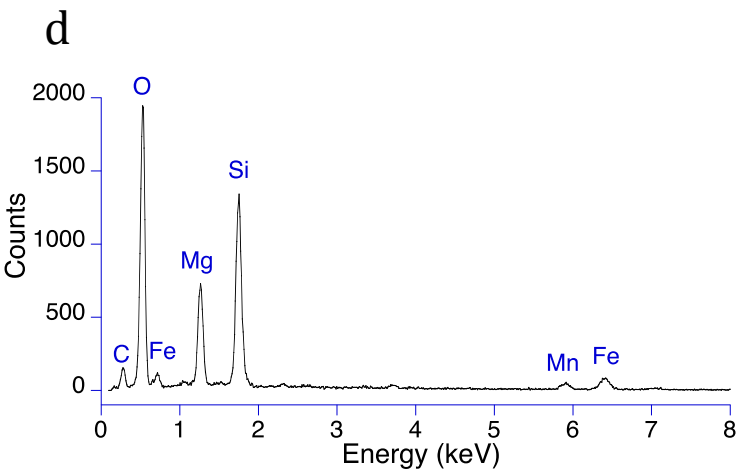
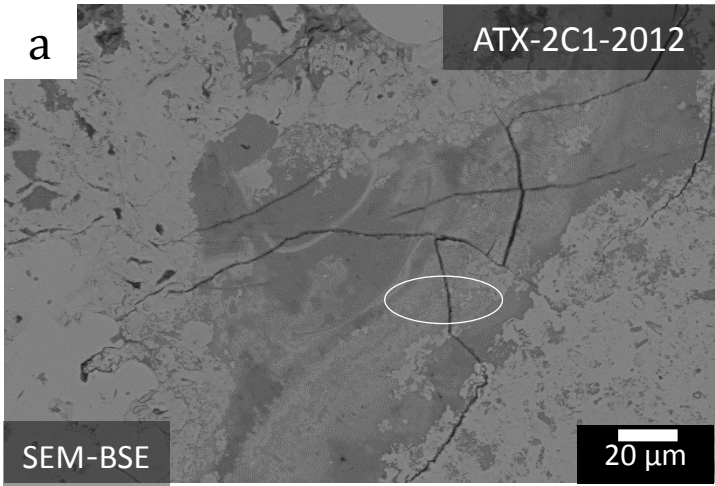




Figure 15

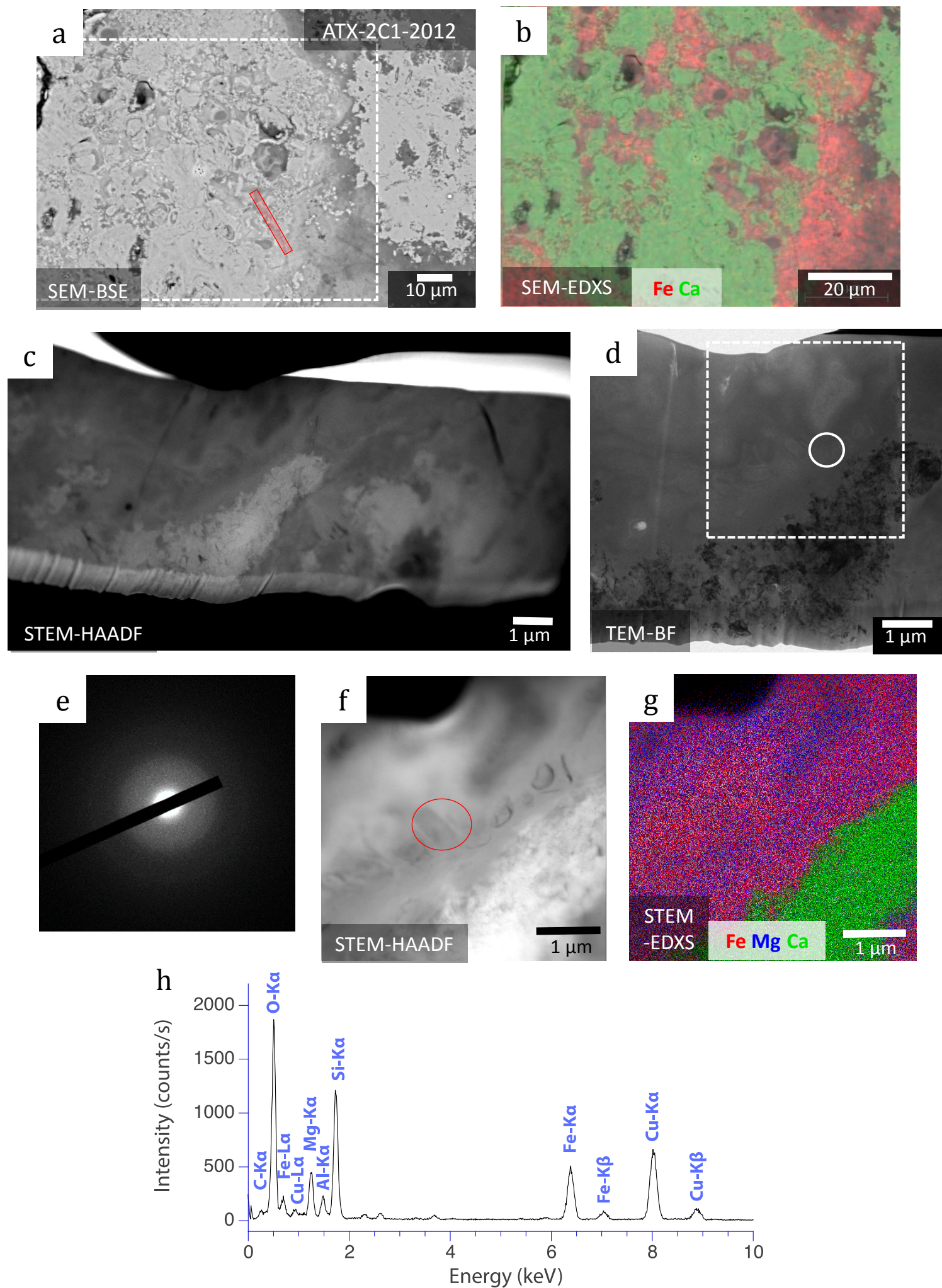


Figure 16

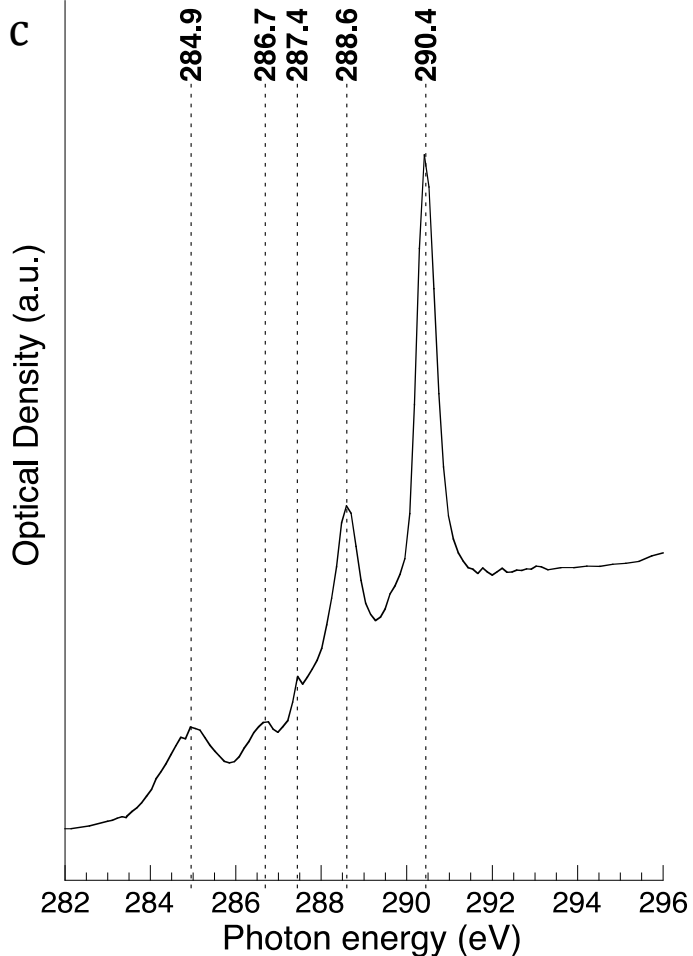
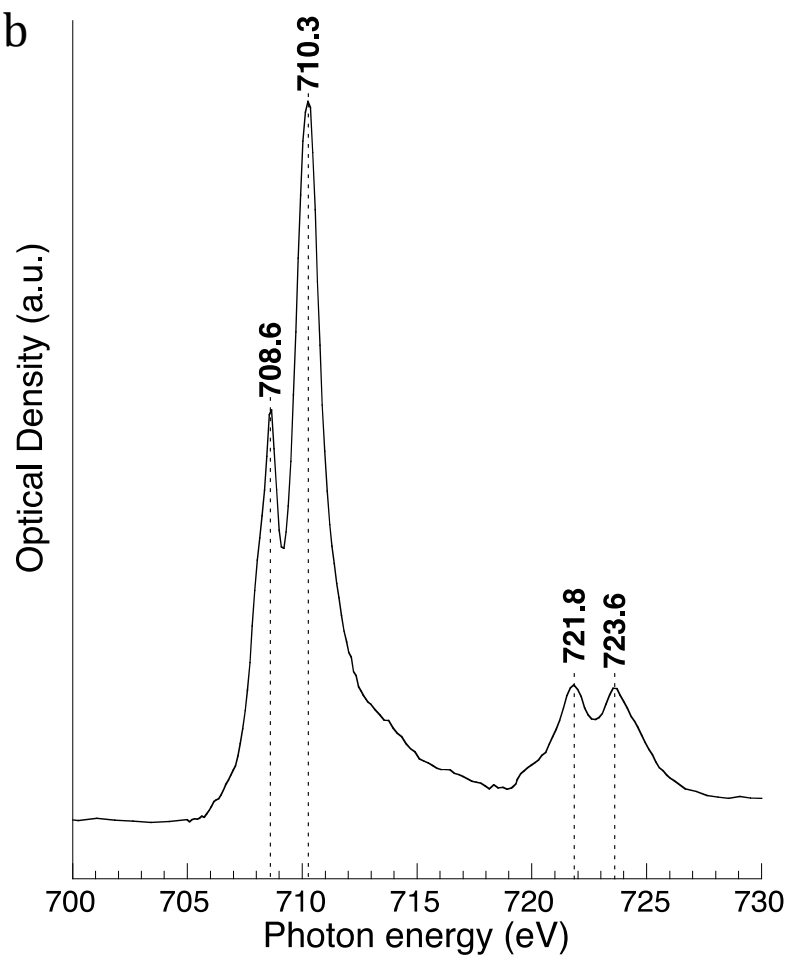
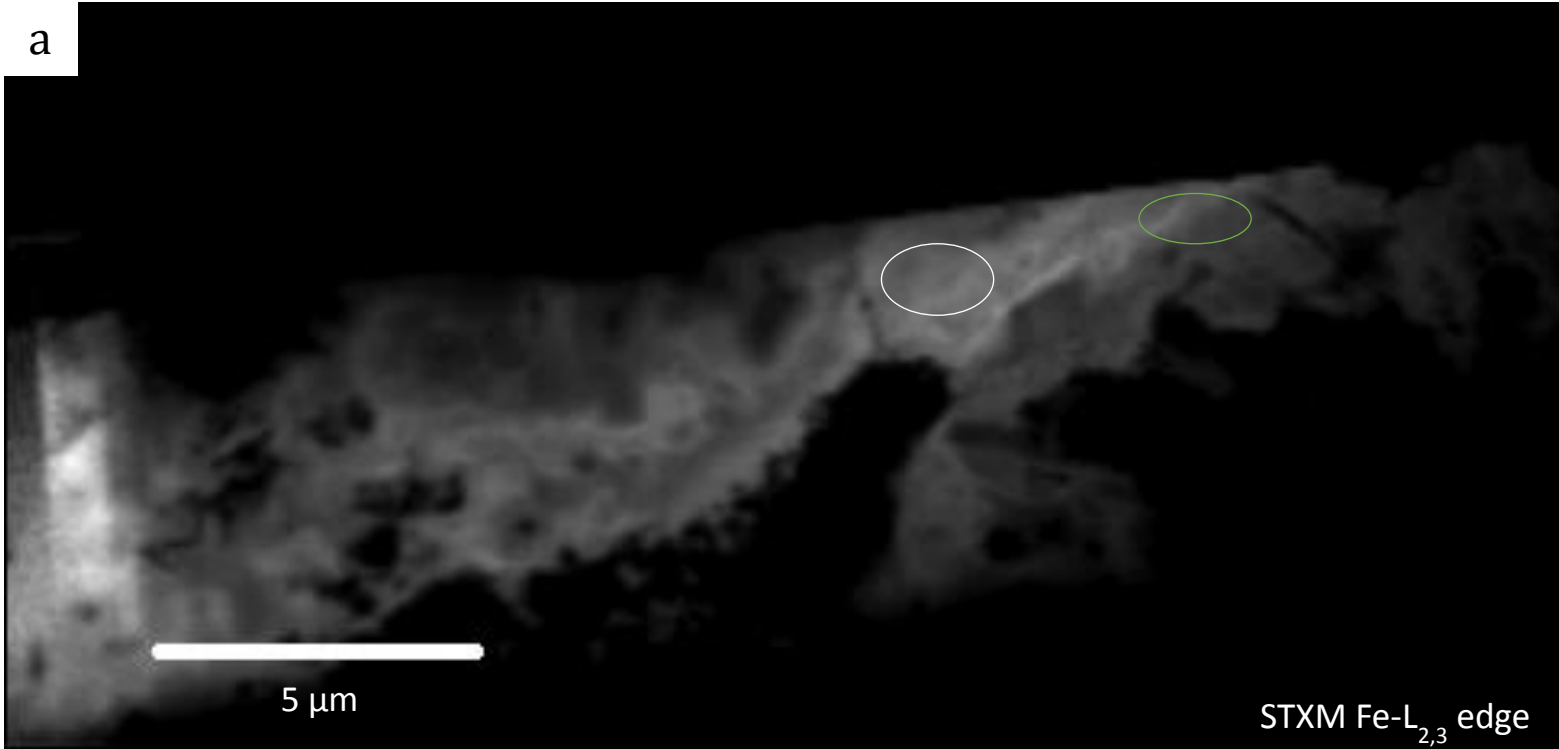
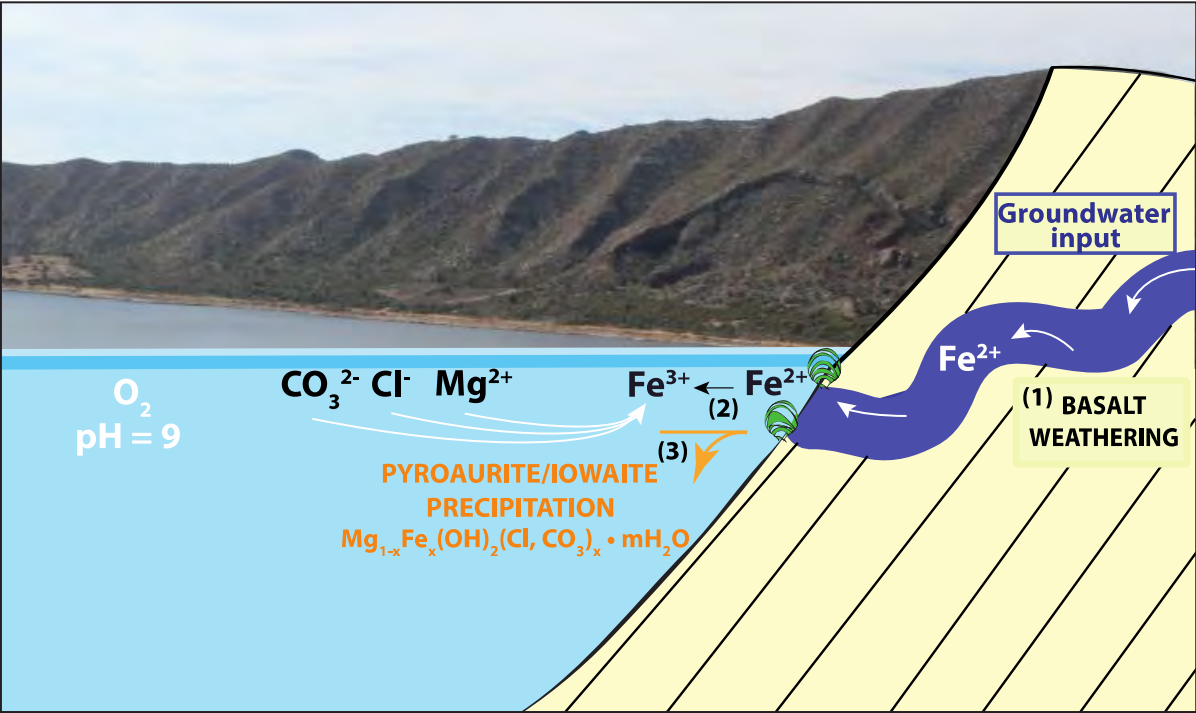




Figure 17



Revised Electronic Annex

[Click here to download Electronic Annex: Revised\\_Supporting-Information.pdf](#)